MSc thesis May 2026

Impacts of S- and X-band Radar Data Assimilation on a Squall-line Event

Huilin Yang

UNIVERSITY OF HELSINKI

Impacts of S- and X-band Radar Data Assimilation on a Squall-line Event

Huilin Yang

30 ECTS thesis approved in partial fulfilment of a double Master degree in Atmospheric Sciences, from Nanjing University and University of Helsinki.

Academic supervisors:

Prof. Kun Zhao

Academic examiners:

Dmitri Moisseev

University of Helsinki

Nanjing University

Nanjing, May 2026

学校代码：10284

分 类 号：P412.25

密　　级：公开

U　D　C：551.5

学　　号：522024380024

南京大学

硕 士 学 位 论 文

论 文 题 目　S 波段与 X 波段雷达资料同化对一次飑线过程的影响

作 者 姓 名　杨惠琳

专业学位类别（领域）　资源与环境

研 究 方 向　雷达资料同化

导 师 姓 名　赵坤教授

2026 年 4 月 9 日

答辩委员会主席	吕迎辉副教授
评　　阅　　人	袁慧玲教授
	明杰副教授
论文答辩日期	**2026 年 5 月 15 日**

研究生签名： 

导师签名： 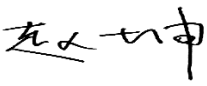



Nanjing University

Master. Dissertation

Impacts of S- and X-band radar data assimilation on a squall-line event

By Huilin Yang

Major：Resources and Environment

Advisor：Prof. Kun Zhao

Nanjing-Helsinki Institute in Atmospheric and Earth System Sciences, Nanjing University

August,2026

南京大学研究生毕业论文中文摘要首页用纸

毕业论文题目：S 波段与 X 波段雷达资料同化对一次飑线过程的影响

资源与环境 专业 2024 级硕士生姓名：杨惠琳

指导教师（姓名、职称）：赵坤 教授

摘要

多普勒天气雷达能够提供高时空分辨率的回波和风场信息，是改进强对流天气分析与预报的重要观测资料。相比常规 S 波段天气雷达，X 波段天气雷达具有空间分辨率高、低层探测能力较强等优势，但其在强对流天气数值预报中的同化应用研究仍相对有限。为评估 X 波段雷达资料对强对流天气分析与预报的影响，本文选取 2024 年 7 月 1 日发生在长江中下游地区的一次典型飑线型强对流过程为研究对象，基于 WRF 模式及其 WRFDA 三维变分同化系统，开展了多波段雷达资料同化试验。

首先，对比了以流函数、势函数为动力控制变量的 CV5 方案和以经向风、纬向风为动力控制变量的 CV7 方案下背景误差协方差的特征，并通过单点试验分析增量特征，并结合背景误差参数敏感性试验，研究发现，CV5 方案形成的分析增量整体较为平滑，更倾向于表征较大尺度背景误差结构；相比之下，CV7 方案对风场结构的响应更直接，形成的分析增量更具局地性和集中性，更有利于保持强对流过程中中低层的中小尺度动力结构。最终确定 CV7 方案及优化后的背景误差参数配置为本文后续正式资料同化试验的较优方案。

在此基础上，开展了控制试验（CTL）、同化 S 波段雷达资料试验（DA_S）和联合同化 S 波段与 X 波段雷达资料试验（DA_S_X），从风场结构、水凝物分析增量、动力场预报、雷达回波预报和降水预报等方面系统评估了额外同化 X 波段雷达径向速度观测的作用。结果表明，联合同化 X 波段雷达径向速度观测后，低层风场和水凝物场均得到了修正，其中 925 hPa 高度层上局地风速高值中心和辐合结构更加清晰，低层雨水混合比和中层霰混合比的局地调整更为明显。

预报结果显示, 试验 DA_S_X 对 925 hPa 风场和 850 hPa 散度场中小尺度结构的模拟优于 CTL 和 DA_S；在组合反射率预报中，DA_S_X 对主回波带连续性、局地强回波中心及内部细节的刻画更接近观测；在逐小时降水预报中，DA_S_X 对条带状降水结构和局地强降水中心的模拟最为合理, 5 mm 和 10 mm 阈值下的 BIAS 和 FSS 评分均为最优, 表明 X 波段雷达资料在强对流天气数值预报中具有较好的应用潜力。

关键词：雷达资料同化；飑线；X 波段天气雷达；S 波段天气雷达

南京大学研究生毕业论文英文摘要首页用纸

THESIS: Impacts of S- and X-band radar data assimilation on a squall-line event

SPECIALIZATION: Resources and Environment

POSTGRADUATE: Huilin Yang

MENTOR: Prof. Kun Zhao

Abstract

Doppler weather radar provides high-spatiotemporal-resolution information on echo structure and wind fields and is an important observational data source for improving the analysis and forecasting of severe convective weather. Compared with conventional S-band weather radar, X-band weather radar has advantages such as higher spatial resolution and stronger low-level detection capability. However, research on the assimilation of X-band radar data in the numerical prediction of severe convective weather remains relatively limited.

To evaluate the impact of X-band radar data on the analysis and forecasting of severe convective weather, this study selected a typical squall-line severe convective event that occurred over the middle and lower reaches of the Yangtze River on 1 July 2024 and conducted multi-band radar data assimilation experiments based on the WRF model and its WRFDA three-dimensional variational data assimilation system. First, the characteristics of background error covariance under the CV5 scheme, which uses streamfunction and velocity potential as dynamical control variables, were compared with those under the CV7 scheme, which uses zonal and meridional wind components as dynamical control variables. Analysis-increment characteristics were then examined through single-observation experiments, together with sensitivity experiments on background error covariance parameters. The results show that the analysis increments produced by the CV5 scheme are generally smoother and tend to

represent larger-scale background error structures. In contrast, the CV7 scheme responds more directly to wind-field structure and produces analysis increments that are more localized and concentrated, making it more favorable for preserving mesoscale and convective-scale dynamical structures in the lower and middle levels during severe convective processes. Accordingly, the CV7 scheme and optimized background error parameter configuration are confirmed as the preferred schemes for the subsequent formal data assimilation experiments in this study.

On this basis, a control experiment (CTL), an experiment assimilating S-band radar data (DA_S), and an experiment jointly assimilating S-band and X-band radar data (DA_S_X) were carried out. The added value of assimilating X-band radar radial velocity observations was systematically evaluated in terms of wind-field structure, hydrometeor analysis increments, dynamical-field forecasts, radar echo forecasts, and precipitation forecasts. The results show that, after the joint assimilation of X-band radar radial velocity observations, both the low-level wind field and the hydrometeor field were improved. In particular, the localized high-wind-speed centers and convergence structures at 925 hPa became clearer, and the localized adjustments of low-level rainwater mixing ratio and midlevel graupel mixing ratio became more evident.

Forecast results further show that DA_S_X performs better than CTRL and DA_S in reproducing the mesoscale and convective-scale structures of the 925 hPa wind field and the 850 hPa divergence field. In the composite reflectivity forecasts, DA_S_X reproduces the continuity of the main echo band, the localized intense echo centers, and the internal structural details more faithfully than the other experiments. In the hourly precipitation forecasts, DA_S_X provides the best simulation of the banded precipitation structure and the localized heavy-rainfall centers. In addition, the BIAS and FSS scores under the 5 mm and 10 mm thresholds are the best among the experiments, indicating that X-band radar data have strong potential for application in the numerical prediction of severe convective weather.

Keywords: radar data assimilation; squall line; X-band weather radar; S-band weather radar

Content

1. Introduction 1
1.1 Research background and significance 1
1.2 Research Progress 3
1.2.1 Studies on Severe Convective Systems over the Middle and Lower Reaches of the Yangtze River 3
1.2.2 Studies on Conventional Radar Data Assimilation 5
1.2.3 Research on the Application of X-band Radar Data Assimilation 8
1.2.4 Research on Background Error Covariance 10
1.3 Research objectives 11
1.4 Research Content and Chapter Arrangement 12
2. Data and Methods 15
2.1 Data 15
2.2 Three-Dimensional Variational Data Assimilation Method 17
2.3 Background Error Covariance Statistical Method 18
2.4 Radar Observation Operator 19
2.5 Forecast Verification Methods 21
2.5.1 Fractions Skill Score (FSS) 21
2.5.2 Bias Score (BIAS) 22
3. Case Study and Experimental Design 22
3.1 Case Description 22
3.1.1 Synoptic Situation 22
3.1.2 Radar reflectivity and Radial Velocity Characteristics 23
3.1.3 Wind Field Retrieval Characteristics 25
3.1.4 Precipitation Evolution Characteristics 27
3.2 Experimental Design 29
4. Impact of Different Control Variable Schemes on Radar Data Assimilation 32
4.1 Introduction to CV5 and CV7 Control Variable Schemes 32
4.2 Characteristics of Background Error Covariance 34

4.3 Impact of Different Control Variable Schemes on Forecast Results 38
4.3.1 Single-Observation Experiments 38
4.3.2 Optimal Length-Scale Parameter 41
4.4 Impact of Different Control Variable Schemes on Forecast Results 43
4.5 Summary 45
5. Impacts of the Joint Assimilation of X-band Radar Data on the Squall-line Case ..46
5.1 Analysis Increments 46
5.1.1 Impact on Wind Field Structure 46
5.1.2 Hydrometeor Analysis Increments 50
5.2 Forecast Results 53
5.2.1 Dynamical Field Forecasts 53
5.2.2 Radar Reflectivity Forecasts 58
5.2.3 Precipitation Forecasts 61
5.3 Summary 65
6. Summary and Outlook 67
6.1 Main Conclusions 67
6.2 Innovations of This Study 69
6.3 Limitations 69
References 71
Acknowledgements 76

1. Introduction

1.1 Research background and significance

The middle and lower reaches of the Yangtze River lie within the East Asian monsoon climate zone and are among the key regions in China where warm-season heavy rainfall and severe convective weather occur frequently. From late spring and early summer through the Meiyu season, this region is prone to persistent precipitation, regional rainstorms, and localized severe convective events under the combined influence of the northward advance of the East Asian summer monsoon, the periodic intensification of the subtropical high, and multiscale weather systems, including low-level shear lines, fronts, and low-level jets. Meanwhile, near-surface warming and enhanced low-level transport of warm, moist air promote the continuous accumulation of atmospheric instability, creating favorable conditions for the initiation, development, and organized evolution of mesoscale and convective-scale systems. As a result, hazardous weather such as short-duration heavy rainfall, thunderstorm gales, and hail occurs frequently in this region.

The middle and lower reaches of the Yangtze River are also characterized by a complex underlying surface, with plains, lakes, river networks, hills, and urban agglomerations distributed across the region. Pronounced terrain undulation and strong spatial heterogeneity in surface thermal properties further increase the complexity of the regional environment. These surface conditions influence not only the thermodynamic and moisture structure of the boundary layer and local circulation patterns, but also the initiation location, intensity, and propagation path of convective systems by modulating low-level convergence and moisture transport. Under rapid urbanization, changes in surface roughness, thermal anomalies, and anthropogenic activities have further altered boundary-layer structure, making severe convective weather in this region more localized, sudden, rapidly evolving, and destructive. Once such events occur, they often trigger secondary disasters, including urban waterlogging, traffic disruption, agricultural losses, and failures in power and communication systems, thereby posing serious threats to regional socioeconomic development and public safety. For example, during 4–8 July 2020, a persistent

extreme rainstorm affected the middle reaches of the Yangtze River, and cumulative precipitation at Bahe Station in Huanggang reached 1006.8 mm (Huang et al., 2021). On 18–19 June 2023, Suzhou experienced a severe rainstorm under the influence of a quasi-stationary Meiyu front, causing serious urban flooding in the main urban area (Cao et al., 2025). Therefore, improving the monitoring, warning, and short-term forecasting of severe convective weather over the middle and lower reaches of the Yangtze River is of great scientific and practical importance.

As one of the most important remote sensing tools for monitoring severe convective weather, Doppler weather radar provides convective-scale information on reflectivity structure, radial velocity, and certain microphysical characteristics. It therefore plays a key role in severe convective weather monitoring, nowcasting, and radar data assimilation in numerical models (Aksoy et al., 2009). At present, S-band dual-polarization Doppler weather radar is widely used in operational practice because of its broad coverage, relatively weak attenuation, and stable observation of mesoscale precipitation systems. These strengths allow it to effectively capture the initiation and evolution of squall lines, heavy-precipitation echoes, and hail-bearing storm cells.

The new-generation S-band dual-polarization Doppler weather radar in China generally operates in the VCP21 volume-scan mode, which includes nine elevation angles and requires approximately 6 min to complete one full volume scan (Zhu et al., 2018). Previous studies have shown that S-band radar observations have been widely assimilated into numerical models and have produced favorable results in improving the analysis of localized heavy-rainfall events and enhancing short-term forecast skill. However, conventional S-band radar still has limitations in resolving the fine-scale structure of mesoscale and convective-scale hazardous weather. These limitations include a relatively long volume-scan interval, restricted detection capability in distant low-level regions, and insufficient representation of rapidly evolving small-scale convective cells and their internal vortical structures (Zhang et al., 2019). For severe convective systems with short life cycles and rapid evolution, these limitations can reduce the effectiveness of observational data in improving both the

analysis and forecast fields.

In contrast, X-band weather radar offers higher spatiotemporal resolution and stronger low-level detection capability. It can provide detailed structural information on precipitation systems at much shorter update intervals, demonstrating strong potential for observing mesoscale and convective-scale severe weather systems. Its high temporal resolution facilitates the timely capture of the initiation, merger, intensification, and decay of convective cells, while its finer spatial resolution is advantageous for identifying localized intense echo cores, low-level convergence structures, and microphysical distribution features. Therefore, X-band weather radar can serve as an important complement to conventional S-band radar by compensating for low-level detection gaps, improving rapid-update observation capability, and enhancing the monitoring of localized severe convective weather (Liu et al., 2014; Song et al., 2022).

Therefore, for typical severe convective weather events over the middle and lower reaches of the Yangtze River, a systematic evaluation of the respective roles of S-band radar and X-band weather radar data in analysis and forecasting, together with an exploration of more effective radar data assimilation strategies, will not only deepen our understanding of severe convective weather forecasting in this region but also provide a scientific basis for the application of emerging weather radar observations in regional numerical prediction.

1.2 Research Progress

1.2.1 Studies on Severe Convective Systems over the Middle and Lower Reaches of the Yangtze River

Short-duration heavy rainfall generally refers to precipitation events that reach high intensity within a short period. In both operational forecasting and research, it is commonly defined using a threshold of hourly precipitation equal to or greater than a specified value. In China's meteorological operations and related studies, hourly precipitation of at least 20 mm is commonly regarded as the lower threshold for short-duration heavy rainfall, and the China Meteorological Administration also uses 20 mm h^{-1} or 50 mm in 12 h as corresponding identification criteria. More intense

short-duration heavy-rainfall events are often closely associated with hazardous convective weather (Chen et al., 2013). Because of their sudden onset, small spatial scale, intense local rainfall, and high disaster-causing potential, such events can readily trigger urban waterlogging, floods in small and medium-sized rivers, flash floods, and geological hazards, thereby posing serious threats to life and property in densely populated and economically developed areas. Previous studies have shown that, under climate change, both the frequency and intensity of extreme precipitation events over the middle and lower reaches of the Yangtze River have generally increased, leading to a corresponding rise in regional flood risk (Pei et al., 2017; Yang et al., 2023). For example, a persistent heavy-rainfall event occurred over the Yangtze–Huaihe River basin in 2020 and caused severe flood disasters, further highlighting the importance of heavy-rainfall monitoring and forecasting in this region (Ding et al., 2021).

The middle and lower reaches of the Yangtze River are among the regions in China most frequently affected by warm-season short-duration heavy rainfall and severe convective weather. Influenced by low-level warm and moist transport, shear lines, fronts, and other multiscale weather systems, this region is prone to organized convection and regional heavy-rainfall events during the warm season. Previous studies have shown that the diurnal variation of warm-season precipitation over the middle and lower reaches of the Yangtze River and adjacent areas exhibits pronounced regional differences. In some areas, a bimodal pattern is observed, with both an early-morning peak and an afternoon peak, and the timing of extreme hourly precipitation also shows marked stage-dependent and intraseasonal variations (Yu et al., 2014; Zhao et al., 2020). This indicates that the formation and evolution of short-duration heavy rainfall in this region are controlled not only by the large-scale circulation background, but also by boundary-layer processes and local thermodynamic conditions.

At present, studies on severe convective weather and short-duration heavy rainfall over the middle and lower reaches of the Yangtze River have mainly focused on climatological characteristics, the evolution mechanisms of mesoscale convective

systems, improvements in numerical simulation, and the application of high-spatiotemporal-resolution observational data (Wang et al., 2014; Qi et al., 2023). Because these processes exhibit pronounced mesoscale and convective-scale characteristics, and because the low-level wind field, convective structure, and hydrometeor distribution directly affect the location and intensity of precipitation, weather radar observations—especially high-spatiotemporal-resolution reflectivity and radial velocity data—are of great value for depicting the internal structure of convective systems and correcting mesoscale thermodynamic and dynamic features in model initial fields. On this basis, assimilating multi-band weather radar data to improve the model representation of the low-level wind field, convective initiation, and precipitation evolution is of great scientific significance and practical value for enhancing the analysis and forecasting of severe convective weather, especially short-duration heavy rainfall, over the middle and lower reaches of the Yangtze River.

1.2.2 Studies on Conventional Radar Data Assimilation

With the development of convective-scale numerical weather prediction, accurately characterizing the initial state of severe convective systems has become one of the key issues in improving forecast skill. Because severe convective weather exhibits pronounced mesoscale and convective-scale characteristics, conventional surface and upper-air observations often fail to adequately capture the internal fine structure and rapid evolution of convective systems, thereby limiting model capability in the analysis and prediction of severe convective weather. Doppler weather radar offers high spatiotemporal resolution, rapid update frequency, and rich observational information, and it can provide observations such as reflectivity and radial velocity that are closely related to precipitation structure and wind-field characteristics. Therefore, incorporating radar observations into the initial fields of numerical models has become one of the major approaches for improving forecasts of severe convective weather (Sun and Crook, 1997; Snyder et al., 2003).

At present, the methods most commonly used for radar data assimilation include the Ensemble Kalman Filter, variational data assimilation methods, and hybrid ensemble–variational methods.The Ensemble Kalman Filter estimates flow-dependent

background error covariance from ensemble forecast samples and can therefore effectively represent the evolving error structure associated with changing weather systems. As a result, it has been widely applied in convective-scale data assimilation (Dowell et al., 2004; Tong and Xue, 2005; Aksoy et al., 2009). Variational data assimilation methods, by contrast, achieve an optimal combination of observational information and background fields by constructing a cost function and solving an optimization problem under specified constraints. Among these methods, four-dimensional variational assimilation can make integrated use of observations at different times within the assimilation window and has achieved good performance in radar data assimilation studies (Sun and Crook, 1994; Xu, 1996; Sun et al., 2010). With the development of data assimilation theory, some studies have further attempted to combine ensemble-based and variational methods in order to retain both the flow-dependent background error covariance of ensemble approaches and the stability of the variational framework (Houtekamer and Mitchell, 1998; Hamill and Snyder, 2000; Gao and Stensrud, 2014). However, such hybrid assimilation methods generally involve high computational cost in high-resolution convective-scale models. In contrast, three-dimensional variational assimilation has clear advantages in computational efficiency, system stability, and operational feasibility, and it therefore remains widely used in regional numerical weather prediction and case studies of severe convective weather (Sun et al., 2010). In addition, through a cycling assimilation strategy, three-dimensional variational assimilation can gradually incorporate newly available observations, thereby compensating to some extent for its lack of an explicit temporal constraint.

In radar data assimilation, radial velocity and reflectivity are the two most commonly used observed variables. Radial velocity is closely related to wind-field structure, and its assimilation technique is relatively mature. It usually improves the dynamical structure of convective systems by adjusting the wind-field distribution in the model initial state, thereby influencing convective initiation, organization, and development (Sun and Crook, 1997; Sun et al., 2010). Previous studies have shown that the simultaneous assimilation of radial velocity and radar reflectivity generally

leads to more effective improvements in the structural analysis of convective systems and enhances short-term precipitation forecast skill. This is particularly evident during the first 0–6 h of the forecast, when such assimilation helps shorten model spin-up time and improves the prediction of precipitation location and intensity (Sun et al., 2010; Wang and Sun, 2013). Overall, radar data assimilation has considerable potential to improve the wind, thermodynamic, and hydrometeor fields in the model initial state, and it has become one of the important approaches for enhancing the numerical prediction of severe convective weather.

In recent years, with the development of high-resolution numerical models and new-generation weather radar observing systems, radar data assimilation research has increasingly advanced toward more refined convective-scale analysis and forecasting. In particular, the application of next-generation weather radar observations with high spatiotemporal resolution has provided a new observational foundation for more accurately depicting the internal structure of severe convective systems. However, assimilation results are strongly affected by the choice of assimilation method, control variable configuration, background error covariance formulation, and observation operator design. At present, the applicability of radar data assimilation to different types of severe convective systems, its effectiveness in improving key mesoscale structures, and its impact on precipitation forecasts still require further investigation.

Over the middle and lower reaches of the Yangtze River, heavy rainfall and severe convective weather are often closely associated with mesoscale convective systems or squall lines, and their initiation and evolution are jointly influenced by multiple factors, including low-level jets, moisture transport, environmental stratification, and topographic conditions (Yu et al., 2014; Ding et al., 2021). Although previous studies have provided relatively in-depth analyses of the structural characteristics and dynamical mechanisms of severe convective systems in this region, research on radar data assimilation—especially the impact of assimilating high-resolution radar observations on the structural evolution of squall-line systems and on precipitation forecasts—remains limited. Therefore, conducting radar data assimilation sensitivity experiments for typical severe convective cases over the

middle and lower reaches of the Yangtze River, and comparing the effects of different assimilation schemes on the model initial field and subsequent forecasts, is of considerable scientific significance and practical value for improving the numerical prediction of severe convective weather, particularly short-duration heavy rainfall, in this region.

1.2.3 Research on the Application of X-band Radar Data Assimilation

Although S-band weather radar has long been widely used to monitor precipitation systems and large-scale weather processes, it still has limitations in depicting the fine-scale dynamical structure of mesoscale and convective-scale severe weather systems. First, because the radar beam rises with increasing distance from the radar, conventional S-band radar has a pronounced observational blind zone in the lower atmosphere. Second, its spatial resolution is relatively limited, making it difficult to fully resolve fine-scale structures within convective systems, such as low-level convergence bands, vortical features, and wind-shear structures that are dynamically important (Zhang et al., 2008; Tao and Zhang, 2014; Kepert, 2018). Previous studies have shown that low-level wind shear and convergence play important roles in the development and maintenance of severe convective systems, whereas conventional S-band radar still has limited capability for observing these low-level features (Xiao et al., 2021).

With the development of new weather radar technologies, X-band radar has attracted increasing attention because of its higher spatial resolution and superior low-level detection capability. Compared with S-band radar, X-band dual-polarization radar can observe the microstructure of precipitation systems in greater detail and has shown strong potential in studies of mesoscale convective systems (Anagnostou et al., 2008). Subsequent studies further indicated that X-band radar has observational capability comparable to, or even better than, that of S-band radar in detecting localized precipitation structures and internal microphysical characteristics of convective systems, while also capturing low-level convective structures more effectively (Diss et al., 2009). In addition, its higher spatial resolution and lower sampling altitude give it clear advantages in low-level observations, allowing it to

compensate effectively for the low-level observational blind zones of S-band radar and thereby improve the monitoring of low-level structures in severe convective weather systems (Wu et al., 2010).

In recent years, X-band radar observations have been widely applied to the study and monitoring of various types of hazardous weather, including hail warning, tornado identification, and analyses of microphysical processes in mesoscale convective systems (Philips et al., 2017; Song et al., 2022). In studies of short-duration heavy rainfall, networked observations using multi-band radar systems have gradually become an important direction of development. By combining X-band radar with conventional S-band radar, it is possible to expand observational coverage while improving spatial resolution, thereby providing more reliable data for quantitative precipitation estimation and severe convective weather monitoring (Huang et al., 2025).

On this basis, some new-generation X-band radars, with faster scanning modes and higher update frequencies, can capture the rapid evolution of convective systems in greater detail. Relevant studies have shown that high-temporal-resolution X-band radar has clear advantages in detecting low-level wind-field structures, the evolution of convective cells, and mesoscale and convective-scale dynamical structures (Morotomi et al., 2020; Cheng et al., 2020). For mesoscale and convective-scale severe weather systems, high-spatiotemporal-resolution observations are essential for resolving their three-dimensional dynamical structure. Studies have shown that X-band radar can effectively observe structures such as convective precipitation systems, squall lines, and mesoscale vortices, and can provide more detailed observational information for retrieving three-dimensional wind fields in severe convective systems (Zhang et al., 2021).

X-band radar observations have also gradually been applied in data assimilation studies for numerical weather prediction. Previous studies have shown that assimilating radial velocity and reflectivity observations from X-band radar can effectively improve the analysis of mesoscale and convective-scale weather system structures and significantly enhance short-term precipitation forecast skill (Honda et

al., 2022). For example, Honda et al. (2022) assimilated X-band radar observations into the simulation of a precipitation event and found a marked improvement in short-term precipitation forecast scores. Further studies have shown that incorporating X-band radar observations into numerical models can improve the analysis of low-level wind-field structure and effectively optimize the predicted location and intensity of precipitation systems (Li et al., 2023). However, the application of the dense X-band radar network deployed over the middle and lower reaches of the Yangtze River to severe convective weather forecasting still requires further investigation.

Therefore, data assimilation studies based on high-spatiotemporal-resolution radar observations are of great importance for improving the numerical prediction of severe convective weather.

1.2.4 Research on Background Error Covariance

In data assimilation systems, especially within the variational assimilation framework, background error covariance (B) is one of the key factors that determine analysis quality. The B matrix not only controls the relative weighting of background information and observations in the analysis, but also determines the spatial spreading of observational increments and the transfer of information among different physical variables. Therefore, the accurate estimation and representation of background error covariance has long been a central issue in variational data assimilation and remains one of the major factors affecting the performance of assimilation systems (Derber and Bouttier, 1999; Bannister, 2008; Brousseau et al., 2011).

From a physical and mathematical perspective, background error covariance plays several important roles. First, the spatial correlation structure of the B matrix determines how observational information is propagated from observation locations to surrounding areas. As a result, in regions with sparse observations, the analysis is particularly sensitive to the specification of B. In other words, the structure of background error covariance largely determines whether limited observations can be effectively projected into the three-dimensional model space (Derber and Bouttier, 1999; Bannister, 2008).

Second, the auto-correlations and cross-correlations contained in the B matrix allow information to spread within the same variable and enable coordinated adjustment among different variables. Consequently, observations can jointly influence model variables such as wind, temperature, and moisture, rather than affecting only the directly observed quantity (Derber and Bouttier, 1999; Bannister, 2008).

In addition, background error covariance directly affects the smoothness of analysis increments and their dynamical balance. Appropriate correlation length scales help suppress local noise and unrealistic small-scale oscillations, thereby improving the continuity and physical consistency of the analysis. At the same time, if the B matrix includes reasonable multivariate balance relationships, it can help maintain consistency among the wind, mass, and thermodynamic fields and reduce the high-frequency adjustment and spurious gravity-wave responses that may occur immediately after assimilation (Bouttier and Courtier, 1999; Derber and Bouttier, 1999). This is particularly important for convective-scale numerical prediction, because severe convective systems have fine-scale structures and evolve rapidly. If the analysis is insufficiently balanced, the model is prone to strong initial adjustment, which can weaken the actual benefit of radar data assimilation.

Background error covariance is usually constructed offline using statistical methods such as the NMC method and is then introduced into the assimilation system through a control-variable transformation. In WRFDA, for example, the formulation of background error covariance and the configuration of control variables directly affect the spatial spread of observational increments and the way different physical variables are adjusted in a coordinated manner. Previous studies have shown that different control-variable schemes perform differently in severe convective cases, and that a reasonable specification of background error covariance can improve the effectiveness of radar data assimilation and enhance convective-scale precipitation forecast skill (Radhakrishnan et al., 2020; Song et al., 2023; Wan et al., 2024).

1.3 Research objectives

This study investigates a typical severe convective weather event over the middle

and lower reaches of the Yangtze River. Based on the WRF model and its WRFDA three-dimensional variational data assimilation system, numerical simulation and data assimilation experiments are conducted using radar and conventional observations. The main objectives are threefold: first, to evaluate the impact of assimilating radar radial velocity and reflectivity data on the model initial fields and short-term precipitation forecasts; second, to compare the extent to which different assimilation schemes improve the structure of severe convective systems and the skill of precipitation forecasts; and third, to examine the potential operational application of radar data assimilation in forecasting severe convective weather over the middle and lower reaches of the Yangtze River, thereby providing a scientific basis for improving the numerical prediction of regional severe convective weather.

1.4 Research Content and Chapter Arrangement

This study investigates a typical squall-line severe convective weather event over the middle and lower reaches of the Yangtze River, with a focus on the assimilation of X-band weather radar data and its impacts on convective-scale analysis and forecasting. To address the rapid evolution of mesoscale and convective-scale structures in severe convective weather, the richness of radar observations, and the insufficient representation of such structures in conventional initial fields, the study employs the WRFDA three-dimensional variational assimilation system to systematically examine how different control-variable schemes and background error covariance settings affect radar data assimilation performance. It further evaluates the extent to which assimilating X-band weather radar data improves the analysis and forecast fields of this squall-line case, with the aim of providing a useful reference for the application of new-generation weather radar observations in the numerical prediction of severe convective weather.

The main contents of this study are as follows. First, in view of the frequent occurrence of severe convective weather and short-duration heavy rainfall over the middle and lower reaches of the Yangtze River, the study reviews previous research on radar data assimilation, the application of X-band weather radar, and background error covariance, and then identifies the key scientific questions and research

objectives to be addressed. Second, it describes the observational data, data quality-control procedures, numerical model, and assimilation methods used in this study, including the WRFDA three-dimensional variational assimilation system, the statistical method for background error covariance, the radar observation operators, and the forecast verification methods. Third, a typical squall-line case over the middle and lower reaches of the Yangtze River is selected and comprehensively analyzed in terms of synoptic conditions, radar reflectivity and radial velocity characteristics, retrieved wind-field features, and precipitation evolution. Based on this analysis, the numerical assimilation experiments are designed.

Furthermore, to address the issue of control-variable configuration in radar data assimilation, the study compares the characteristics of background error covariance and the responses of analysis increments under different control-variable schemes. Idealized single-observation experiments are then conducted to examine the effects of these schemes on the assimilation results and to determine the optimal values of the length-scale parameters. On this basis, real-data assimilation experiments using X-band weather radar observations are carried out. Particular attention is given to the characteristics of the analysis increments in the wind and hydrometeor fields after assimilation, and the extent to which assimilation improves the forecast of this squall-line case is systematically evaluated in terms of the dynamical field, radar echo, and precipitation prediction.

The dissertation is organized into six chapters, as follows.

Chapter 1, Introduction. This chapter presents the research background and significance, reviews previous studies on radar data assimilation, the application of X-band weather radar, and background error covariance, and then clarifies the research objectives, main contents, and overall structure of this dissertation.

Chapter 2, Data and Methodology. This chapter introduces the observational data used in this study and their quality-control procedures. It also describes the WRFDA three-dimensional variational assimilation method, the statistical method for background error covariance, the radar observation operators, and the forecast verification methods, thereby providing the methodological foundation for the

subsequent experiment design and result analysis.

Chapter 3, Case Description and Experimental Design. This chapter presents the selected case and analyzes the event in terms of the synoptic situation, radar reflectivity and radial velocity characteristics, retrieved wind-field features, and precipitation evolution. It also describes the model-domain configuration, physical parameterization schemes, and the design of the assimilation experiments.

Chapter 4, Impacts of Different Control-Variable Schemes on Radar Data Assimilation. This chapter introduces the two control-variable schemes, CV5 and CV7, analyzes their background error covariance characteristics, and compares the differences in analysis increments under the two schemes through idealized single-observation experiments. It further determines the optimal values of the length-scale parameters.

Chapter 5, Impacts of Assimilating X-band Radar Data on the Squall-line Case. Based on the optimized control-variable scheme and background error parameters, this chapter analyzes the characteristics of the analysis increments in the wind and hydrometeor fields after assimilating X-band weather radar data. It then compares and evaluates the experimental results in terms of dynamical-field forecasts, radar echo forecasts, and precipitation forecasts.

Chapter 6, Conclusions and Prospects. This chapter summarizes the main conclusions of the study, outlines its innovations, analyzes its limitations, and discusses directions for future research.

2. Data and Methods

2.1 Data

Data assimilation experiments require multiple types of input data, including model background fields, observational datasets, and background error statistics. In the WRFDA system, the model background is first generated from the WRF preprocessing and forecasting components, while observational data are processed and converted into formats suitable for assimilation. Together with the background error covariance, these inputs are introduced into the WRFDA system to produce an analysis field, which is then used as the initial condition for subsequent WRF forecasts. The basic workflow of the WRFDA data assimilation system is shown in Figure 2-1.The datasets used in this study include radar observations, precipitation observations, and reanalysis data. Radar observations are used as the main assimilation data and diagnostic basis for convective structure analysis; precipitation observations are used for forecast verification; and reanalysis data provide the initial and lateral boundary conditions for the numerical model.

（1）Radar Datasets

This study utilizes weather radar observations from 00:00 to 20:00 on July 1, 2024, in the middle and lower reaches of the Yangtze River (MLRYR). The dataset comprises base data from nine S-band Doppler weather radars and five X-band weather radars. S-band observations are primarily sourced from the China New Generation Weather Radar (CINRAD) operational system, featuring a maximum detection range of approximately 460 km and 11 elevation levels. X-band radar data is mainly used to provide supplementary low-level coverage with 10 elevation levels. To ensure the reliability of data assimilation and diagnostic analyses, all radar base data underwent rigorous quality control (QC) before use. These procedures included outlier removal, identification and elimination of non-meteorological echoes, data consistency checks, and format conversion to enhance the validity and utility of the observations. The radar stations are concentrated in Jiangsu Province and its surrounding areas (117.15°E-120.98°E, 31.90°N-34.65°N), covering the core regions of severe convective activity in the MLRYR and the Jianghuai area. Radar

observations serve both as inputs for data assimilation experiments and as the basis for analyzing the structural characteristics and evolutionary processes of severe convective systems.

（2）Precipitation Observations

To evaluate the improvements in precipitation forecasting from numerical simulations and assimilation experiments, this study employs ground-based precipitation data from a dense network of automatic weather stations (AWSs) in Jiangsu Province. These data are provided by the Jiangsu Provincial Automatic Meteorological Observation Network and feature a 1-hour temporal resolution. The high station density across the province facilitates the quantitative evaluation of short-duration heavy rainfall (SDHR) forecasts.

（3）Reanalysis Data

The model is driven by the Final (FNL) reanalysis data provided by NCEP/NCAR, sourced from the Global Data Assimilation System (GDAS). The FNL dataset has a 6-hour temporal resolution, a 0.25°×0.25° horizontal resolution, and 34 vertical pressure levels. These data provide the initial and lateral boundary conditions required to drive the WRF model for numerical simulations.

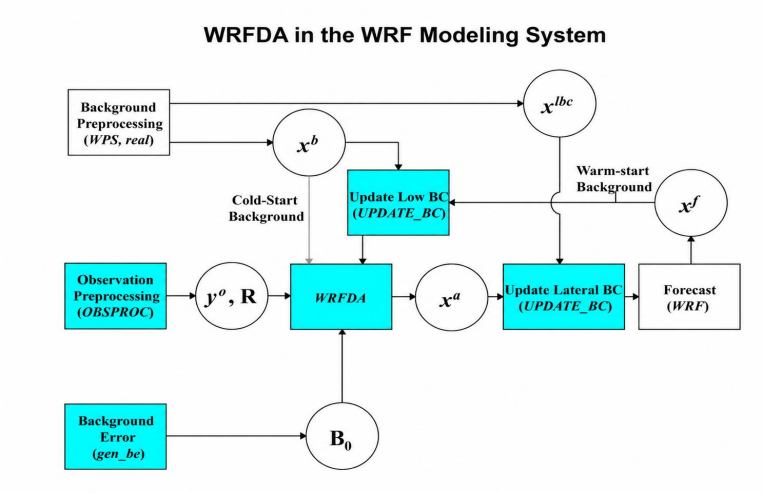

Figure 2-1. Schematic diagram of the basic workflow of the WRFDA data assimilation system (blue boxes indicate components of the data assimilation system). Adapted from the WRFDA User's Guide.

2.2 Three-Dimensional Variational Data Assimilation Method

The fundamental principle of data assimilation involves merging observational information with the background field provided by a numerical model to produce an analysis field that more accurately reflects the actual state of the atmosphere. This analysis field then serves as the initial condition for subsequent numerical weather predictions. WRFDA (WRF Data Assimilation) is a specialized data assimilation system designed for the WRF model and is widely utilized in regional numerical weather prediction and related academic studies. The system supports several methodologies, including 3DVar, 4DVar, and hybrid assimilation. Among these, 3DVar is frequently employed in convective-scale data assimilation research and operational systems due to its high computational efficiency and robust implementation stability. This study utilizes the WRF-4.2.1 model alongside the WRFDA V4.6.1 system to conduct data assimilation experiments based on the 3DVar framework.

In the 3DVar framework, the optimal integration of observations and the model background is achieved by minimizing a specific objective function. The objective function for three-dimensional variational assimilation is typically expressed as follows:

$$J(x) = \frac{1}{2}(x - x_b)^T B^{-1}(x - x_b) + \frac{1}{2}[y_0 - H(x)]^T R^{-1}[y_0 - H(x)] \quad (2\text{-}1)$$

Where x, x_b, and y_0 represent the analysis, background, and observation variables, respectively. The matrices B and R denote the background error covariance and observation error covariance, while H represents the observation operator that maps model variables from the model space to the observation space. By minimizing this objective function, an optimal analysis field can be obtained that simultaneously satisfies the background information and the observational constraints.

The background error covariance matrix (B matrix) is a critical factor influencing the effectiveness of the assimilation. Theoretically, B matrix is a high-dimensional, non-diagonal symmetric matrix that is difficult to store or solve directly in practical computations. To reduce computational complexity and enhance

efficiency, the WRFDA system adopts the incremental variational assimilation method and decomposes the background error covariance using a Control Variable Transform (CVT). Within this incremental framework, the analysis increment is defined as: $\delta x = x - x_b = Uv$, Where x is the analysis field, x_b is the background field, v is the control variable, and U is the control variable transformation matrix satisfying the relationship.

$B = UU^T$. Consequently, the objective function can be reformulated as:

$$J(v) = \frac{1}{2}v^T v + \frac{1}{2}(d - H'Uv)^T R^{-1}(d - H'Uv) \quad (2\text{-}2)$$

In this equation, H' represents the linearized observation operator, R is the observation error covariance matrix, and $d = y_0 - H(x_b)$ is the innovation vector, which represents the difference between the observations and the background-simulated observations. This variable transformation decomposes the high-dimensional background error covariance matrix into several manageable transformation matrices, which significantly reduces the computational load and enables the minimization of the objective function.

The WRFDA 3DVar system offers three primary control variable schemes for the background error covariance: CV5, CV6, and CV7. CV5 is the default scheme, utilizing stream function and unbalanced velocity potential as momentum control variables, while also including unbalanced temperature, pseudo-relative humidity, and unbalanced surface pressure. In contrast, the CV7 scheme directly employs horizontal wind components as momentum control variables, replacing the stream function and velocity potential with zonal and meridional wind components to more directly describe the wind field structure. Because CV7 more effectively characterizes the wind field in convective-scale assimilation, it has seen increasing application in radar data assimilation research in recent years.

2.3 Background Error Covariance Statistical Method

In variational data assimilation systems, the background error covariance matrix characterizes the statistical characteristics of model background field errors. It is a key factor for the effective propagation of observational information. Because the true

atmospheric state is difficult to obtain directly, the background error covariance is usually estimated via statistical methods.

This study utilizes the NMC method to construct the background error covariance matrix. This method approximates model background errors by calculating the differences between forecasts with different lead times. Specifically, we obtain a set of background error samples by differencing forecasts valid at the same time but with different lead times (e.g., 24-hour versus 12-hour forecasts). Following this approach, we selected twice-daily forecast results from June 1 to June 30, 2024, as the statistical samples. Through statistical analysis of this dataset, we derived the variances and covariance structures for each control variable, which were then used to construct the B matrix within the WRFDA system.

During the implementation process, the WRFDA system decomposes the background error covariance through the Control Variable Transform (CVT). This transform converts the complex, large-scale covariance matrix into several manageable statistics, which effectively reduces computational complexity. Furthermore, this method reflects the dynamic and thermodynamic balance relationships between variables to a certain extent. This allows observational information to propagate across different physical quantities, thereby improving the physical consistency of the assimilation analysis.

In the data assimilation experiments of this study, we adopted the CV7 control variable scheme within the WRFDA system. This scheme uses horizontal wind components (u,v) as momentum control variables, combined with temperature (T), pseudo-relative humidity (RHs), and surface pressure (Ps). Compared to traditional schemes that use stream function and velocity potential as momentum variables, CV7 directly characterizes wind field structures. Consequently, it demonstrates superior applicability for convective-scale data assimilation research.

2.4 Radar Observation Operator

In radar data assimilation, the radial velocity observed by Doppler weather radar reflects the movement of airflow along the radar's line of sight. We must construct appropriate observation operators to link radar observations with model variables.

This study adopts a direct radial velocity assimilation method. The fundamental approach involves calculating the simulated radial velocity by projecting the model's three-dimensional wind field onto the radar's line of sight. The expression for the observation operator is:

$$V_r = u\frac{x - x_i}{r_i} + v\frac{y - y_i}{r_i} + (w - v_T)\frac{z - z_i}{r_i} \tag{2-3}$$

$$v_T = 5.4a \cdot q_r^{0.125} \tag{2-4}$$

In these equations, (u, v, w) represent the three-dimensional wind speed components. (x, y, z) denotes the position of the radar station, while (x_i, y_i, z_i) represents the position of the radar observation volume. r_i is the distance between the observation point and the radar. v_T is the terminal fall velocity of precipitation particles ($m \cdot s^{-1}$). q_r denotes the rainwater mixing ratio ($g \cdot kg^{-1}$). a is a correction factor defined as:

$$a = \left(\frac{p_0}{p}\right)^{0.4} \tag{2-5}$$

In this formula, p represents the base-state pressure and p_0 represents the surface pressure.

Unlike radial velocity, this study does not employ a direct assimilation scheme for radar reflectivity, but instead adopts an indirect reflectivity assimilation approach. Its basic framework is consistent with the indirect assimilation method implemented in WRFDA by Wang et al. (2013), in which reflectivity is not directly introduced into the variational system but is instead used to construct pseudo-observations related to humidity and hydrometeors. In addition, the hydrometeor retrieval component incorporates the background-dependent method proposed by Chen et al. (2020, 2021) to improve the physical consistency of pseudo-observation construction.

Wang et al. (2013) proposed an indirect assimilation method for radar reflectivity. This approach first retrieves the rainwater content and related humidity information from the radar reflectivity and then assimilates them as observations. In this scheme, the equivalent radar reflectivity factor Z_e integrates the contributions from rainwater

(q_r), snow (q_s), and graupel (q_g):

$$Z_e = Z(q_r) + Z(q_s) + Z(q_g) \tag{2-6}$$

The calculation employs corresponding empirical formulas based on the ambient temperature. For water vapor estimation, when the radar reflectivity factor exceeds 30 dBZ, we assume the air inside the cloud is saturated with a relative humidity of 100%. We then calculate the corresponding water vapor specific humidity q_v based on the local pressure and temperature. This value is introduced into the assimilation system as an "observation":

$$q_v = rh \times q_{vs} \tag{2-7}$$

In this equation, rh represents the relative humidity and q_{vs} is the saturated water vapor specific humidity. This indirect method accounts for the contributions of ice-phase particles to radar reflectivity during the calculation process.

2.5 Forecast Verification Methods

2.5.1 Fractions Skill Score (FSS)

The Fractions Skill Score (FSS), as proposed by Roberts and Lean (2008), is a neighborhood-based verification metric that evaluates the spatial consistency of precipitation forecasts by incorporating spatial scale information. This method statistically analyzes precipitation occurrence within a designated neighborhood window by applying uniform weighting to all grid points, which allows for the calculation of spatial probability characteristics.

Specifically, the precipitation occurrence frequencies for both the model forecast and observation fields are calculated within each neighborhood window. These frequencies are then used to derive the Fractional Brier Score (FBS):

$$FBS = \frac{1}{N}\sum_{N}(P_{fcst} - P_{obs})^2 \tag{2-8}$$

Where N denotes the total number of neighborhood windows within the study domain, while P_{fcst} and P_{obs} represent the forecasted and observed precipitation fractions in each window, respectively. The FSS is subsequently calculated based on the FBS:

$$FSS = 1 - \frac{FBS}{\frac{1}{N}(\sum_N P_{fcst}^2 - \sum_N P_{obs}^2)} \tag{2-9}$$

FSS values range from 0 to 1. When the FSS approaches 1, it indicates that the forecast and observations exhibit high spatial consistency, representing superior predictive skill. Conversely, a value near 0 indicates poor performance. As the neighborhood radius or the number of windows increases, the spatial distribution of precipitation probability becomes smoother, which typically leads to an increase in FSS values.

2.5.2 Bias Score (BIAS)

The Bias Score (BIAS) is used to assess the overall systematic deviation of the model regarding the frequency of precipitation. It is defined as the ratio of the number of forecasted precipitation events to the number of observed events. This indicator reflects the extent to which the model overestimates or underestimates precipitation occurrences.

The calculation formula is as follows:

$$BIAS = \frac{H + F}{H + M} \tag{2-10}$$

In this formula, H represents hits, referring to cases that precipitation is observed and correctly predicted by the model; M represents misses, which refers to instances where precipitation was observed but not predicted by the model.

When the BIAS value is 1, the forecasted frequency is consistent with the observed frequency. A BIAS greater than 1 indicates that the model overestimates precipitation events, while a BIAS less than 1 signifies that the model underestimates the frequency of precipitation.

3. Case Study and Experimental Design

3.1 Case Description

3.1.1 Synoptic Situation

A typical squall-line severe convective event occurred over the middle and lower reaches of the Yangtze River on 1 July 2024. To examine the large-scale synoptic background of this event, Figure 3-1 presents the 500 hPa geopotential height and

wind field at 00:00, 06:00, 12:00, and 18:00 UTC on 1 July 2024.

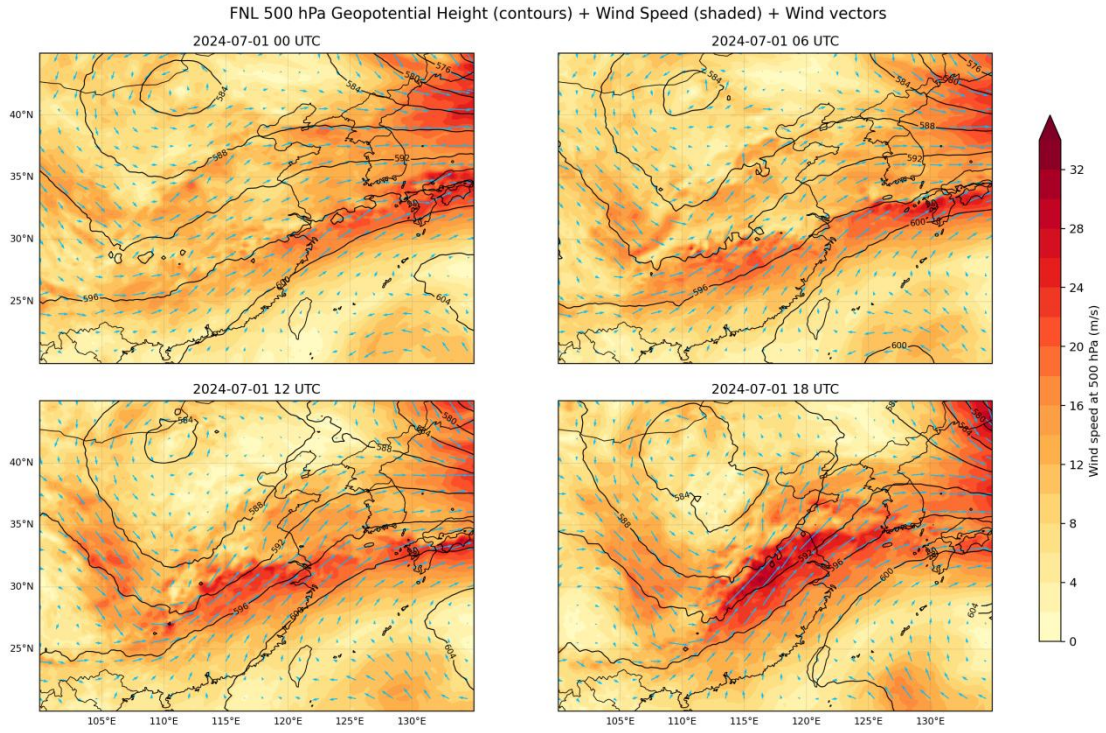

Figure 3-1 500 hPa geopotential height and wind field at 00:00, 06:00, 12:00, and 18:00 UTC on 1 July 2024.

As shown in Figure 3-1, the study region remained under a prevailing westerly flow throughout the event. The mid- to upper-level winds over the middle and lower reaches of the Yangtze River were relatively strong, indicating a well-established steering flow. From 00:00 to 18:00 UTC, the westerly flow persisted and gradually strengthened. In particular, the high-wind-speed zone became more pronounced near the study area at 12:00 and 18:00 UTC, indicating that favorable upper-level dynamical conditions were maintained during the development of the event. Meanwhile, the geopotential height field was generally zonal, suggesting that the study region was situated within a stable large-scale westerly circulation background. Such a synoptic configuration provided favorable large-scale conditions for the organization, maintenance, and eastward propagation of the squall-line system.

3.1.2 Radar reflectivity and Radial Velocity Characteristics

Figure 3-2 illustrates a comparison of the plan reflectivity and radial velocity for a single radar at station Z9523 at 13:02 Beijing Time (BJT) on July 1, 2024, showing both the raw data (left column) and the quality-controlled results (right column) at a selected elevation angle. The top panels, (a) and (b), display the reflectivity factor (Z);

both effectively characterize the southwest-to-northeast banded structure of the strong echoes within this severe convective system near the Yangtze River Delta. These intense echoes are primarily concentrated in the central and northern regions of the study area, with localized intensities exceeding 45 dBZ, which indicates the presence of strong convective cores within the system. Compared to Figure 3-1(a), panel (b) demonstrates significant suppression of weak echoes and isolated noise through the application of a higher reflectivity threshold and filtering techniques. This results in clearer boundaries for the banded features and convective cores, as well as a more coherent overall structure, suggesting that the quality control and visualization enhancements primarily improve the readability and interpretability of the convective patterns.

The bottom panels, (c) and (d), present the radial velocity (V_r) field. Using a masking strategy consistent with the reflectivity panels, the velocity field exhibits the characteristic pattern of alternating positive and negative velocities. Prominent velocity gradients are observed in the vicinity of the strong echoes, reflecting significant wind shear and localized dynamic adjustments within and surrounding the convective system. After applying the quality control procedures synchronized with Figure 3-2(b), the velocity patches in panel (d) appear smoother with fewer discrete artifacts. However, the large-scale dipole distribution and the relative positions of the high- and low-velocity regions remain largely unchanged. This indicates that while the processing successfully suppresses noise and improves spatial consistency, it does not fundamentally alter the underlying broad-scale dynamical structure. In general, the strong spatial correlation between the high-reflectivity zones and the regions of intense radial velocity gradients highlights the close relationship between low-level wind field inhomogeneities, localized convergence, and the development of the convective system.

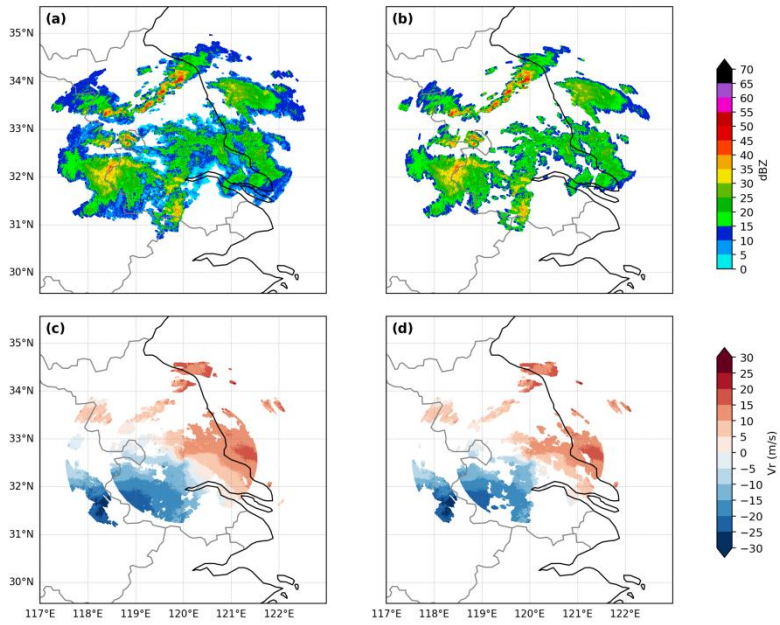

Figure 3-2. PPI images from the Z9523 (11 elevation angles in the volume scan; the lowest tilt is shown) weather radar at 13:02 Beijing Time on 1 July 2024: (a)(b) reflectivity factor Z and (c)(d) radial velocity Vr ($m \cdot s^{-1}$). The left column is before quality control, and the right column is after quality control.

3.1.3 Wind Field Retrieval Characteristics

To further examine the three-dimensional dynamical structure of this event, wind-field retrievals were performed using multi-radar observations. Figure 3-3 shows the retrieved wind field and the corresponding reflectivity distribution at approximately 1 km altitude at 14:00 on 1 July 2024. A pronounced low-level airflow convergence zone is evident near the intense echo band, indicating that the low-level wind-field configuration played an important role in convective development.

Figure 3-4 further presents the wind-field distributions at 1, 2, 3, and 4 km at 14:00 on 1 July 2024. Overall, the convergence signature is strongest at 1 km, suggesting that convective initiation and low-level dynamical forcing were concentrated near the surface and around the top of the boundary layer. At 2–3 km, the wind field gradually transitions from localized convergence to a more organized regional airflow pattern, indicating that the midlevel wind field contributed substantially to system maintenance. By 4 km, the wind field becomes smoother and localized convergence weakens, suggesting that the upper portion of the system was primarily controlled by the environmental flow. This vertical structure indicates that

the event exhibited a typical dynamical configuration characterized by low-level convergence and midlevel maintenance, providing an observational reference for evaluating whether the model can reproduce this structure in subsequent analyses.

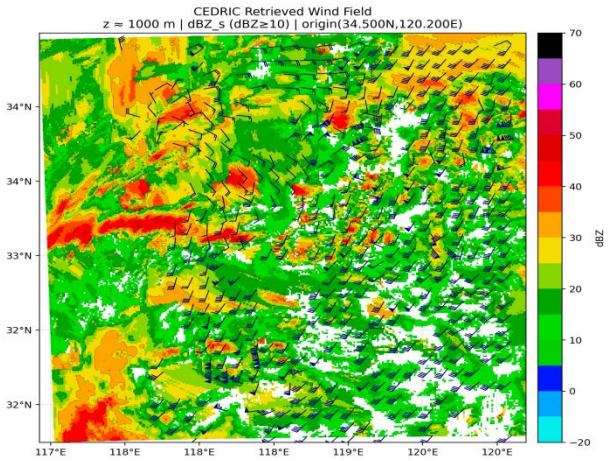

Figure 3-3. Multi-radar retrieved wind field and reflectivity distribution at a height of approximately 1 km.

The wind-field organization in this event was mainly concentrated in the lower and middle levels, with the most pronounced convergence occurring at 1 km, while a certain degree of mesoscale organization was still maintained at 2–3 km.

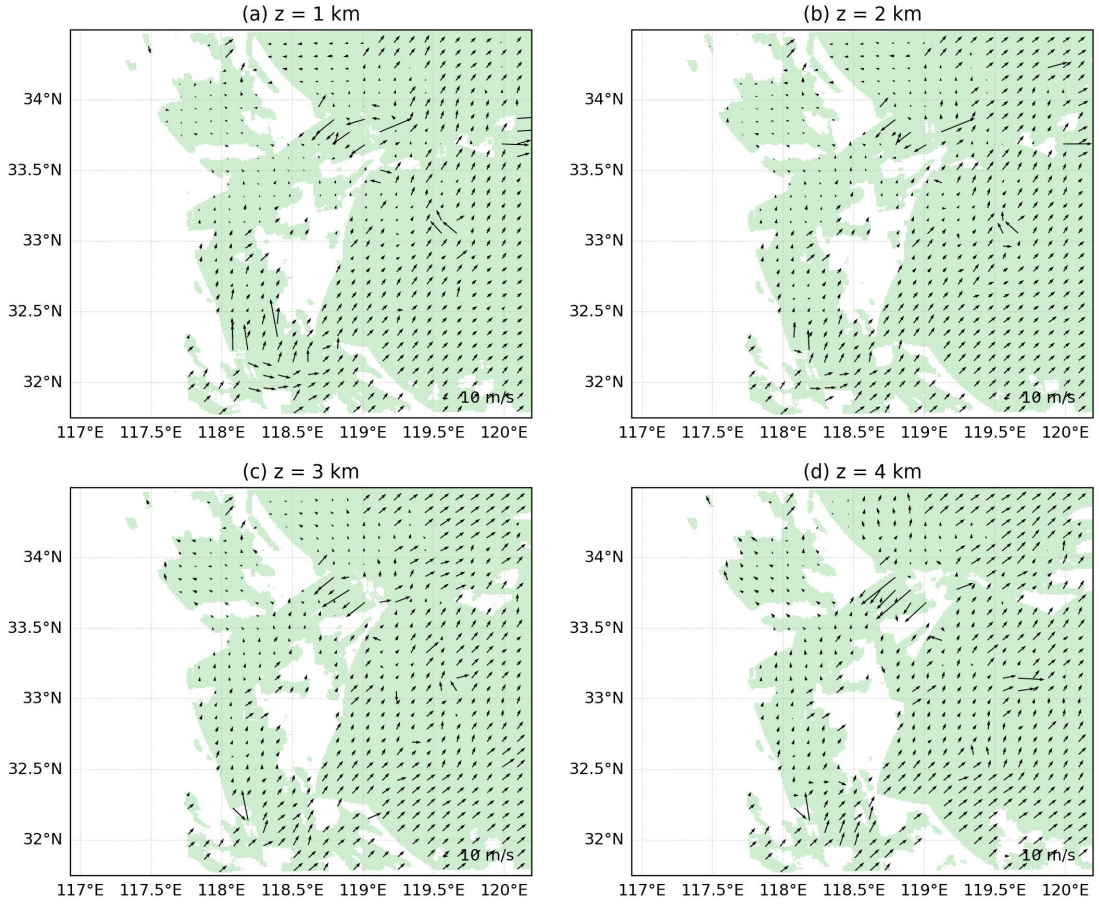

Figure 3-4. Horizontal wind fields at 1–4 km: (a) 1 km, (b) 2 km, (c) 3 km, and (d) 4 km. Arrows denote horizontal wind vectors.

3.1.4 Precipitation Evolution Characteristics

Figure 3-5 shows the hourly distribution of surface-station precipitation from 12:00 to 23:00 on 1 July 2024. It can be seen that the precipitation in this event exhibited a distinct banded distribution, with the heavy-rainfall centers aligned along a southwest–northeast orientation and gradually shifting eastward or northeastward during the evolution of the system, indicating strong organization and persistence. The observed 1 h precipitation shown in Figure 3-5 indicates that the heavy rainfall was mainly distributed along the banded convective system and was most pronounced during 15:00–17:00. The local precipitation maxima correspond well to the intense echo band, suggesting that this severe convective event was characterized by pronounced short-duration heavy rainfall. In terms of spatiotemporal evolution, the main precipitation centers gradually advanced downstream as the convective system

as a whole moved eastward, indicating that this event not only had a clear convective structure but also exhibited good continuity in precipitation evolution. These features provide an observational basis for subsequent comparisons of precipitation location, precipitation-center position, and precipitation-band continuity among different experiments.

In terms of temporal evolution, from 12:00 to 14:00, the precipitation mainly appeared as relatively scattered convective rainfall, and the areas of heavy-rainfall centers were still limited. However, several localized intense rainfall cores had already emerged, indicating that the convective system had begun to develop and gradually become organized. From 15:00 to 17:00, the precipitation intensified rapidly and evolved into a relatively complete band of heavy rainfall. The number of heavy-rainfall centers increased markedly, and the continuity of the precipitation band was significantly enhanced. This indicates that this period represented the most active stage of the event and the period during which short-duration heavy rainfall was most pronounced. From 18:00 to 21:00, the main precipitation band shifted farther eastward and maintained relatively strong rainfall intensity in some local areas, suggesting that the system still had strong maintenance capability during its mature stage. After 22:00, precipitation intensity weakened markedly, the number of heavy-rainfall centers decreased, and the precipitation band gradually narrowed and became more fragmented, indicating that the event had entered its weakening and dissipation stage.

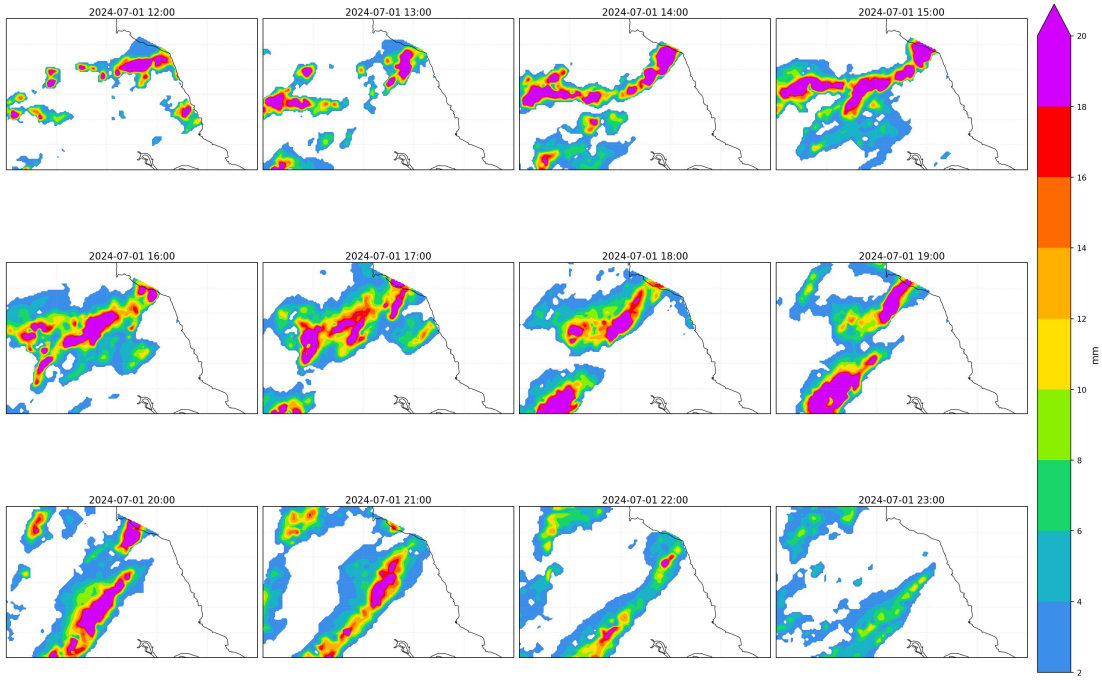

Figure 3-5. Spatio-temporal evolution of observed hourly precipitation.

In terms of spatial structure, the heavy-rainfall area was not uniformly distributed. Instead, multiple localized maxima were embedded along the main precipitation band, reflecting a typical precipitation structure of a mesoscale convective system characterized by "a banded main body with localized intense centers." This precipitation pattern is consistent with the organized convective bands commonly seen in severe convective weather events and further indicates that the event exhibited clear mesoscale-system characteristics. Overall, this precipitation event was characterized by strong suddenness, pronounced locality, a high degree of organization, and relatively long duration, making it well suited as a case for severe convective numerical simulation and radar data assimilation experiments.

3.2 Experimental Design

To investigate the impacts of radar data assimilation and control variable schemes on the analysis and forecasting of the squall line event that occurred in the middle and lower reaches of the Yangtze River on July 1, 2024, this study conducts numerical experiments using the WRF-ARW model and the WRFDA three-dimensional variational (3DVar) system. All experiments are performed under a unified model configuration and background field. We analyze the influence on model

results from two perspectives: the assimilation methodology (by varying control variable schemes) and the observation data (by varying the assimilated data types).

The model employs a double-nested domain configuration. The outer domain (d01) has a horizontal resolution of 9 km and is designed to characterize the large-scale environmental fields. The inner domain (d02) features a 3-km horizontal resolution, which focuses on the regions in and around Jiangsu Province prone to severe convection; this domain is utilized to simulate the meso- and small-scale structures of the squall line system. We implement two-way nesting between the domains to ensure effective information interaction across different scales. As illustrated in the radar station distribution (Figure 3-6), nine S-band radars and five X-band radars are primarily located within or near the inner domain. The significant spatial overlap between the observation coverage and the model grid provides a robust foundation for multi-radar data assimilation.

Regarding the physical parameterization of the model, we maintain consistent configurations across all experiments. The microphysics is represented by a scheme specifically suited for severe convection simulations, while the parameterizations for the planetary boundary layer, surface layer, land surface, and radiation remain identical. Given that the 3-km resolution of the inner domain reaches the convective scale, we deactivate the cumulus parameterization in this domain to explicitly resolve convective processes. This approach allows for a more realistic simulation of the development and evolution of the squall line.

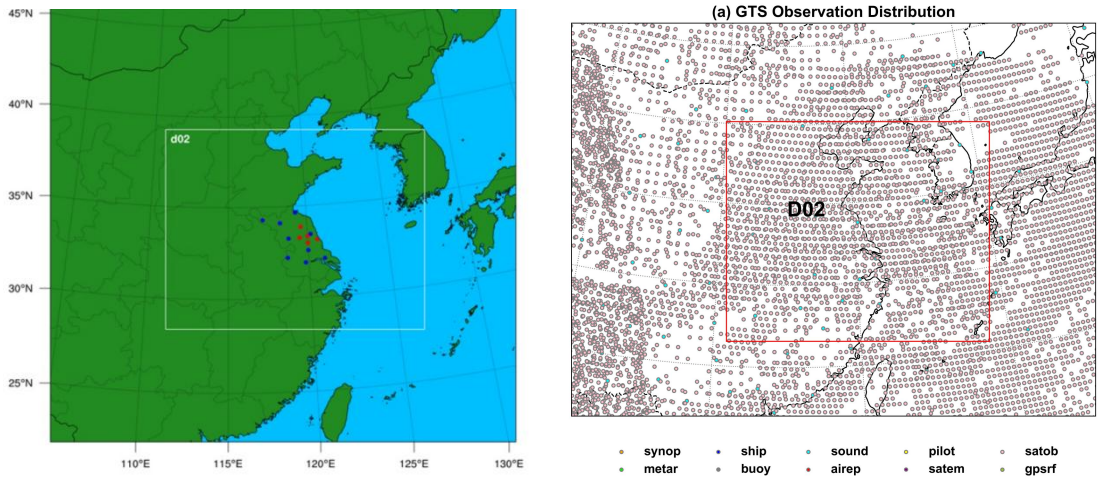

Figure 3-6. Model domains, radar site distribution, and observational coverage. (a) Two-way nested model

domains and radar sites used in this study. (b) Inner model domain (d02) and the coverage of observational data.

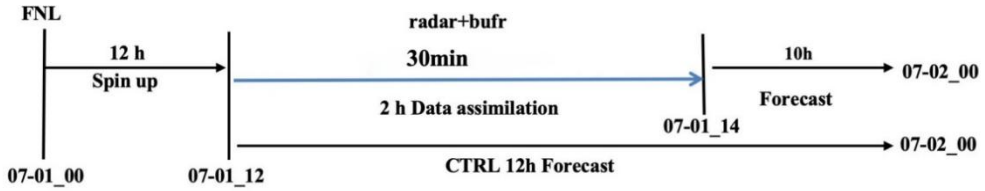

Figure 3-7. Schematic diagram of the data assimilation and forecast experiment procedure.

To systematically assess the impacts of different control variable schemes and radar data configurations, this study designs two categories of experiments. The first category consists of sensitivity experiments for control variable schemes, which analyze how different schemes (CV5 and CV7) and background error covariance parameters influence the analysis increment structures and assimilation performance. In these tests, the type of assimilated data remains constant while the control variable schemes and associated parameters are varied to identify the optimal configuration for this specific case.

Building on these results, we further conduct comparative experiments for radar data assimilation to evaluate the impact of different radar datasets on the simulation and forecasting of the squall line. This category includes three groups: a control experiment (CTRL), an experiment assimilating only S-band radar data (DA_S), and an experiment jointly assimilating S-band and X-band radar data (DA_S_X). The CTRL experiment involves no radar data assimilation and serves as the baseline. The DA_S group assimilates only S-band observations during the cyclic window, whereas the DA_S_X group incorporates both S-band and X-band data under identical conditions. Aside from the observation types, all model settings and assimilation procedures are kept consistent across these three groups.

Furthermore, regarding forecast verification, in addition to analyzing the structural characteristics of the simulated radar echoes, we utilize hourly precipitation observations from automatic weather stations (AWS) in Jiangsu Province for quantitative evaluation. These stations are densely distributed across the study area (Figure 3-8), which effectively captures the spatial patterns of regional precipitation and provides a reliable basis for assessing the performance of various experimental

schemes.

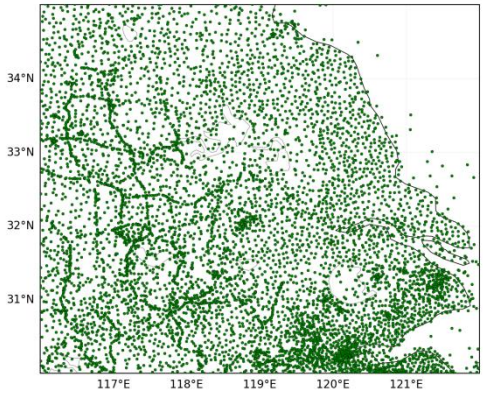

Figure 3-8. Distribution of automatic weather stations in Jiangsu Province.

The green dots in the figure represent the locations of the AWS sites. This dataset is primarily used for hourly precipitation analysis and the verification of numerical precipitation forecasts. The high station density throughout Jiangsu Province ensures an accurate representation of the spatial distribution of regional rainfall.

Based on the experimental design described above, Chapter 4 examines the effects of control variable schemes and background error covariance parameters on assimilation performance, while Chapter 5 evaluates the impact of X-band radar data assimilation in a squall-line case. This framework is used to assess how different assimilation configurations affect the analysis and forecast results.

4. Impact of Different Control Variable Schemes on Radar Data Assimilation

4.1 Introduction to CV5 and CV7 Control Variable Schemes

In the WRFDA three-dimensional variational (3DVar) data assimilation system, the background error covariance is incorporated into the variational solver through the Control Variable Transform (CVT). The fundamental principle is to represent the analysis increment δx in the model space as the product of a control variable v and a transformation matrix U, defined as:

The matrix U is typically decomposed into three components: physical, vertical, and horizontal transformations. These components characterize the statistical balance between variables and the spatial correlation structures of errors.

Within WRFDA, different control variable schemes employ distinct physical transformations. CV5 is a widely used traditional scheme that utilizes the stream function (ψ), unbalanced velocity potential (χ_u), unbalanced temperature (T_u), pseudo-relative humidity (RH_s), and unbalanced surface pressure ($P_{s,u}$) as control variables. Under this scheme, the unbalanced components of the velocity potential, temperature, and surface pressure are obtained by subtracting the balanced portions associated with the stream function from the total field. These transformations are expressed as follows:

$$\chi_u(i,j,k) = \chi(i,j,k) - \alpha_{\psi\chi}(i,j,k)\,\psi(i,j,k) \tag{4-1}$$

$$T_u(i,j,k) = T(i,j,k) - \sum_{l=1}^{N_k} \alpha_{\psi T}(i,j,k,l)\,\psi(i,j,l) \tag{4-2}$$

$$P_{s,u}(i,j) = P_s(i,j) - \sum_{l=1}^{N_k} \alpha_{\psi P_s}(i,j,l)\,\psi(i,j,l) \tag{4-3}$$

In these equations, i and j denote horizontal grid points, while k and l represent vertical levels. The term α represents the regression coefficients between variables, and the subscript u indicates the unbalanced component.

The defining feature of CV5 is the use of statistical regression to decompose variables like temperature and surface pressure into balanced and unbalanced components. This approach introduces strong dynamic balance constraints into the analysis increments. The primary advantage is that the analysis fields usually exhibit good smoothness and consistency, which is suitable for modeling mesoscale background error covariances. However, this scheme has clear limitations. CV5 does not establish direct correlations between the unbalanced velocity potential and temperature or surface pressure. Furthermore, the humidity variable lacks a complete multivariate coupling with other control variables. Consequently, the ability of the system to propagate observational information to the divergent wind and localized, rapidly evolving structures is relatively restricted. For severe convective processes that feature significant convergence or divergence, these constraints may hinder the recovery of fine-scale wind field details during assimilation.

In contrast to CV5, the CV7 scheme directly adopts the horizontal wind components u and v as momentum control variables. These components form the control variable vector along with temperature (T), pseudo-relative humidity (RH_s), and surface pressure (P_s):

$$v_{CV7} = (u, v, T, RH_s, P_s)^T \tag{4-4}$$

4.2 Characteristics of Background Error Covariance

The role of the background error covariance (B matrix) extends beyond merely determining the magnitude of analysis increments; more importantly, it governs the spatial spreading of observational information and the propagation paths between different physical variables. In a three-dimensional variational (3DVar) framework, if the B matrix accurately characterizes the statistical relationships among the wind, thermal, and moisture fields, observational information can be propagated via these correlations to variables that are not directly observed, thereby improving the overall structure of the analysis field. Conversely, if these inter-variable correlations are inadequately constructed, both the range and the direction of information propagation will be restricted.

Under the CV5 framework, the primary characteristic of the background error covariance is the construction of balance relationships centered on the stream function. Because the balanced portions of temperature and surface pressure are primarily contributed by the stream function, observational information propagates more readily through rotational wind correlation structures. Consequently, the impact on divergent wind and divergence structures remains relatively indirect. While this structure helps maintain the smoothness and consistency of analysis fields under large-scale or balanced atmospheric conditions, its ability to represent rapidly evolving, fine-scale structures in mesoscale severe convective processes may be limited.

In comparison, CV7 directly utilizes u and v as momentum control variables, enabling the background error covariance to respond more directly to wind field details. Since it no longer relies on the $\psi - \chi$ decomposition to represent momentum

variables, CV7 more effectively preserves mesoscale features such as low-level convergence lines, local wind shear, and abrupt changes in wind vectors. This characteristic is particularly vital for squall-line convective processes, as the triggering, maintenance, and propagation of such systems are highly dependent on low-level wind configurations and local dynamic structures. Theoretically, the background error covariance associated with CV7 is better suited for recovering local wind fields in convective-scale data assimilation.

In addition to variable balance relationships, the spatial correlation scale of the background error covariance is a critical characteristic. A larger horizontal correlation length scale results in a wider influence range for analysis increments generated by a single observation, leading to smoother analysis fields. However, excessively large scales may cause information to propagate too far, thereby weakening localized strong signals. Conversely, while smaller scales allow analysis increments to better reflect local structures, scales that are too small may lead to fragmented increment distributions that hinder the formation of a continuous and physically reasonable analysis field. Consequently, for severe convection cases, the background error covariance must achieve a balance between "smoothness" and "localization".

For the case investigated in this study, the effectiveness of radar data assimilation depends directly on whether the background error covariance can reasonably represent the relationship between the low-level wind field and the local convective environment. Because squall-line processes exhibit distinct mesoscale organizational features and the evolution of echo bands is closely linked to the position of convergence lines, differences in control variable schemes will ultimately manifest as differences in the structure of the resulting analysis increments. One scheme may tend to produce smooth, large-scale increments, while another may better highlight localized strong signals and wind field details. For these reasons, this study further compares the response characteristics of CV5 and CV7 through single-observation ideal experiments and sensitivity tests of the length-scale parameter to determine the background error covariance configuration most suitable for this research.

Figures 4-1 and 4-2 show the vertical modes and eigenvalue distributions of background error covariance estimated using the CV5 and CV7 schemes, respectively. The two schemes exhibit clear differences in the vertical distribution and decay characteristics of the error modes. Under the CV5 scheme, the error modes associated with momentum-related variables are generally smoother, indicating that this scheme tends to represent background error structures at larger scales. In contrast, under the CV7 scheme, the error modes in the lower and middle levels better reflect local perturbation characteristics, and the eigenvalue decay is more favorable for retaining information related to local low-level wind-field adjustments.

For the severe convective systems investigated in this study, refined characterization of the low-level wind field is critical for recovering convergence, shear, and local transport structures. Consequently, considering the representation capability of the background error modes themselves, CV7 is theoretically more aligned with the requirements of convective-scale data assimilation.

As shown in Figures 4-1and 4-2, the CV5 and CV7 schemes exhibit substantial differences in the vertical error modes and eigenvalue decay characteristics. The error modes in the CV5 scheme are generally smoother and are therefore more suitable for representing larger-scale background error structures. In contrast, the CV7 scheme is more favorable for retaining local wind-field perturbations in the lower and middle levels, which is more consistent with the dominant role of localized dynamical structures in severe convective systems.

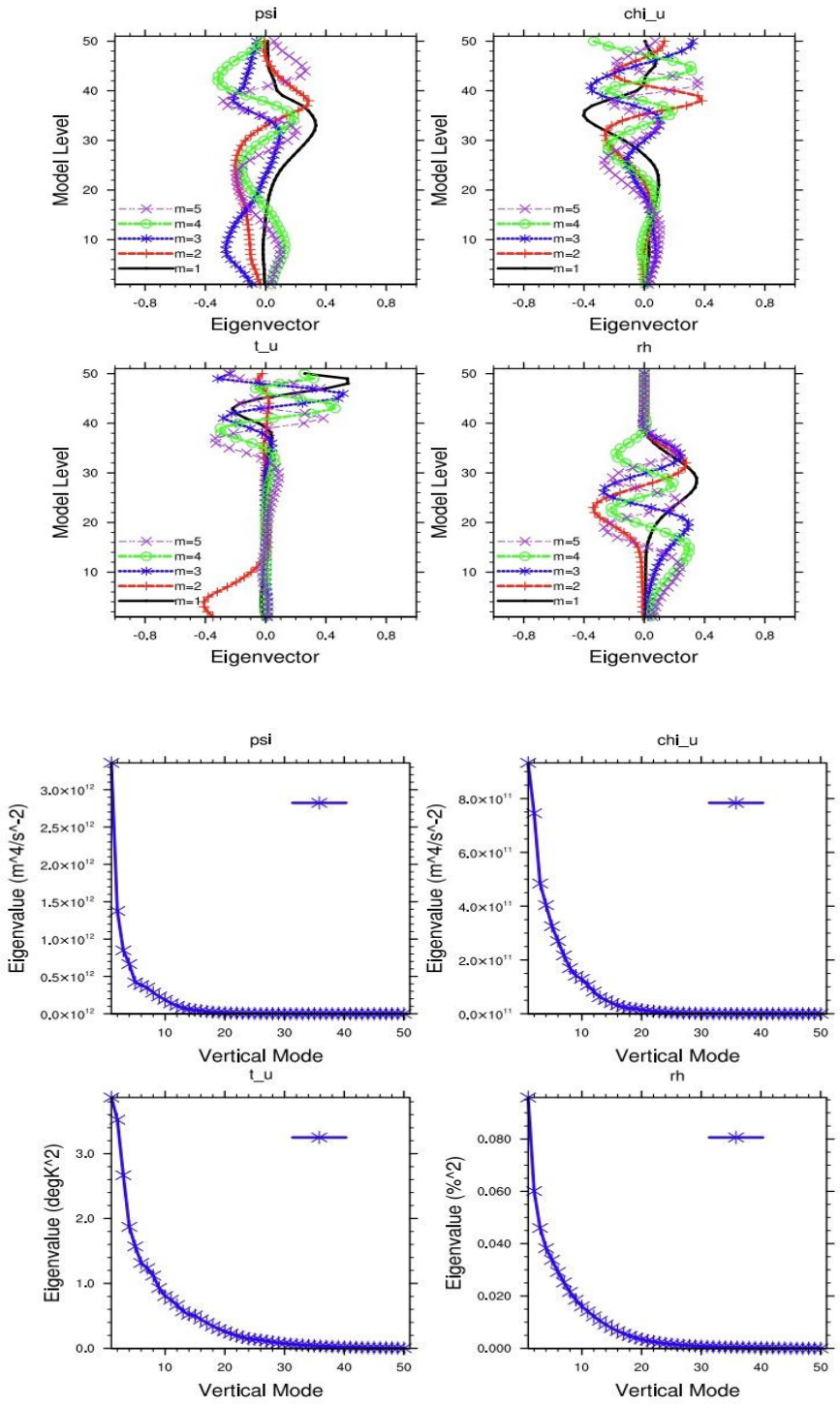

Figure 4-1. Vertical eigenmodes and eigenvalue distributions of the CV5 scheme after the background error covariance statistics.

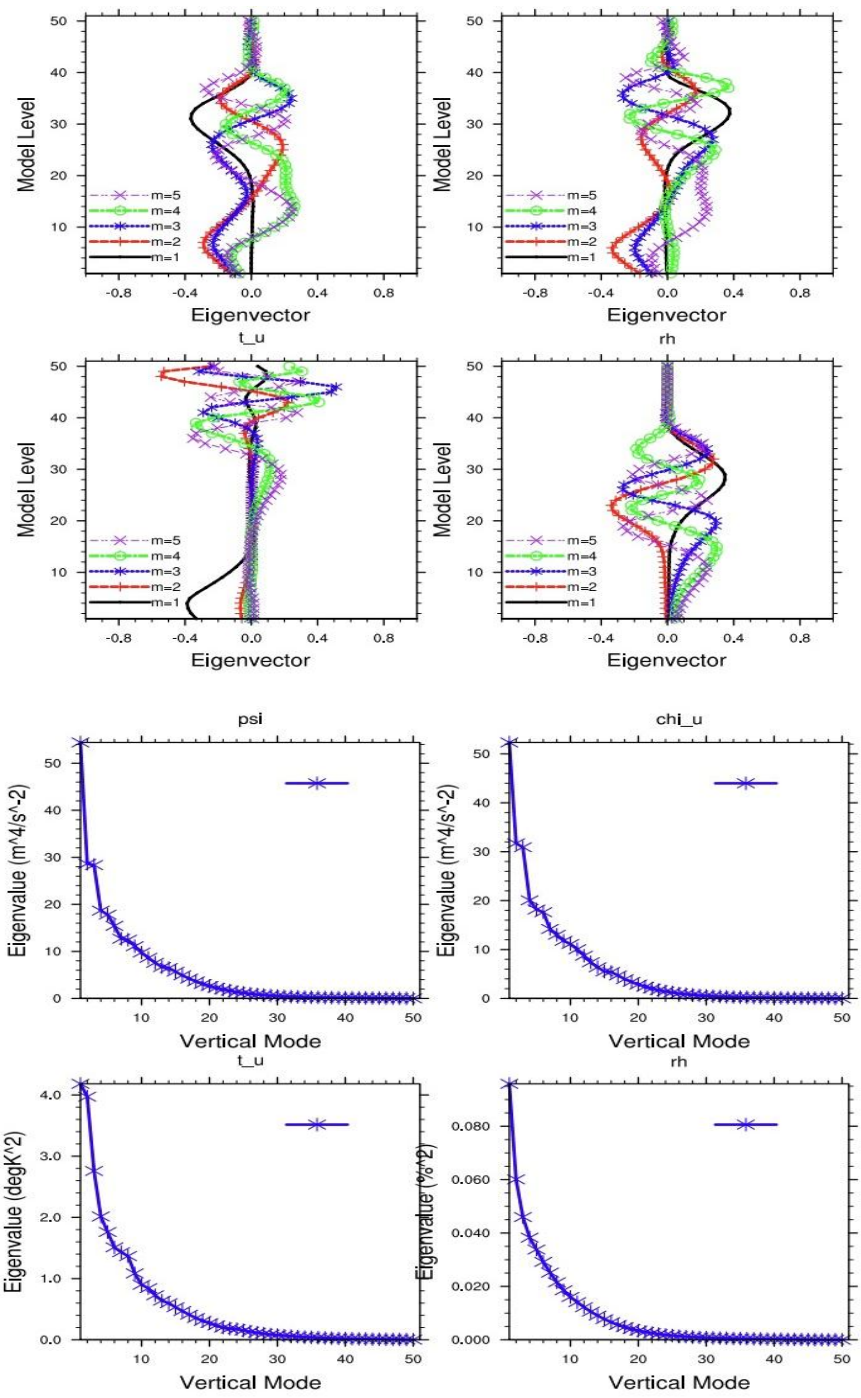

Figure 4-2. Vertical eigenmodes and eigenvalue distributions of the CV7 scheme after the background error covariance statistics.

4.3 Sensitivity Experiments of Background Error Parameters

4.3.1 Single-Observation Experiments

To further analyze the influence of the background error covariance on the propagation of observational information under different control variable schemes,

and to provide a basis for selecting appropriate schemes and parameters for subsequent radar data assimilation experiments, this study conducted single-observation ideal experiments. Unlike real-world assimilation involving multiple stations and time steps, these experiments retain only one radar observation record from the actual station Z9250. This simplified setup highlights the role of the background error covariance itself and facilitates a clearer comparison of the analysis increment structures generated by different control variable schemes.

The observation used in this experiment was read through a standard WRFDA ASCII radar observation file, where total_number = 1 for station Z9250. Notably, this experiment utilizes a single record from a real radar station rather than a synthetic perturbation manually applied to model grid points. Since all experiment groups use the same background field, observation location, and observation data, any differences in the range and structure of the analysis increments primarily reflect the impact of the control variable schemes and background error parameter settings themselves, rather than variations in observation position or intensity.

The primary objective of the single-observation experiments is to examine the control exerted by the background error covariance over the propagation of observational information under highly simplified conditions. For the squall-line convective process investigated in this study, the low-level local wind field structure, convergence configuration, and mesoscale dynamic features are critical for the triggering and organizational development of the system. Therefore, conducting idealized experiments with a real single-station observation helps analyze the differences between control variable schemes in characterizing local dynamic structures.

Figure 4-3 displays the spatial distributions of analysis increments for relative humidity, temperature, u-wind, v-wind, and wind speed at the 14th model level under the CV5 and CV7 schemes. Under identical observation conditions and horizontal length-scale parameters, the characteristics of the analysis increments produced by the two control variable schemes exhibit significant differences.

First, regarding the relative humidity and temperature increments, the CV5 scheme generates a large-scale response structure. Significant positive and negative response zones for relative humidity appear in the northern and southern parts of the research area, while the temperature increment displays a smooth dipole distribution with a broad center and obvious spatial extension. This indicates that under the CV5 background error covariance, information from a single radar observation not only propagates to the wind field but also significantly affects the thermal and moisture fields through statistical balance relationships. In contrast, the relative humidity and temperature increments under the CV7 scheme are markedly weaker and remain near zero, showing only a minimal background response. This suggests that the indirect adjustment of thermal and moisture fields by CV7 is relatively limited.

Second, the differences between CV5 and CV7 are more pronounced in the wind field increments. For the u-wind increment, both CV5 and CV7 exhibit positive increment centers near the observation area, but the CV7 center is more concentrated and localized, whereas the CV5 increment is broader and smoother. For the v-wind increment, CV5 produces a typical large-scale dipole structure that extends over a wide area, while CV7 mainly shows a localized negative increment center with an influence range significantly smaller than that of CV5. The wind speed increment further demonstrates that both schemes adjust the wind speed near the observation point, but CV7 forms a more compact and focused increment center, while CV5 exhibits stronger smoothing and diffusion characteristics.

Under the same len_scaling = 0.3 condition, these differences primarily reflect the impact of the control variable scheme itself on the propagation of observational information rather than the effects of the correlation length scale. Because CV5 utilizes the stream function and associated unbalanced variables to construct the control variable space, observational information propagates more easily over a larger range through balance relationships, leading to a wider increment range. CV7 directly uses u and v as momentum control variables, which effectively constrains the observational information to the vicinity of the observation area, making the wind field adjustments more localized and targeted.

For the squall-line convective case studied here, the low-level local wind field structure and convergence configuration play a vital role in convection triggering, echo organization, and the location of heavy precipitation. The single-observation experiments indicate that although CV5 produces more significant responses in the temperature and moisture fields, its influence range is excessively large. This can lead to the over-diffusion of observational information, which is detrimental to characterizing the localized and rapidly evolving mesoscale structures within severe convection. In contrast, the increment response of the CV7 scheme in the wind field is more concentrated and possesses a more reasonable range, which aligns better with the small-scale and highly localized nature of convective processes. Therefore, this study concludes that CV7 is more suitable for the subsequent radar data assimilation experiments of this squall-line case.

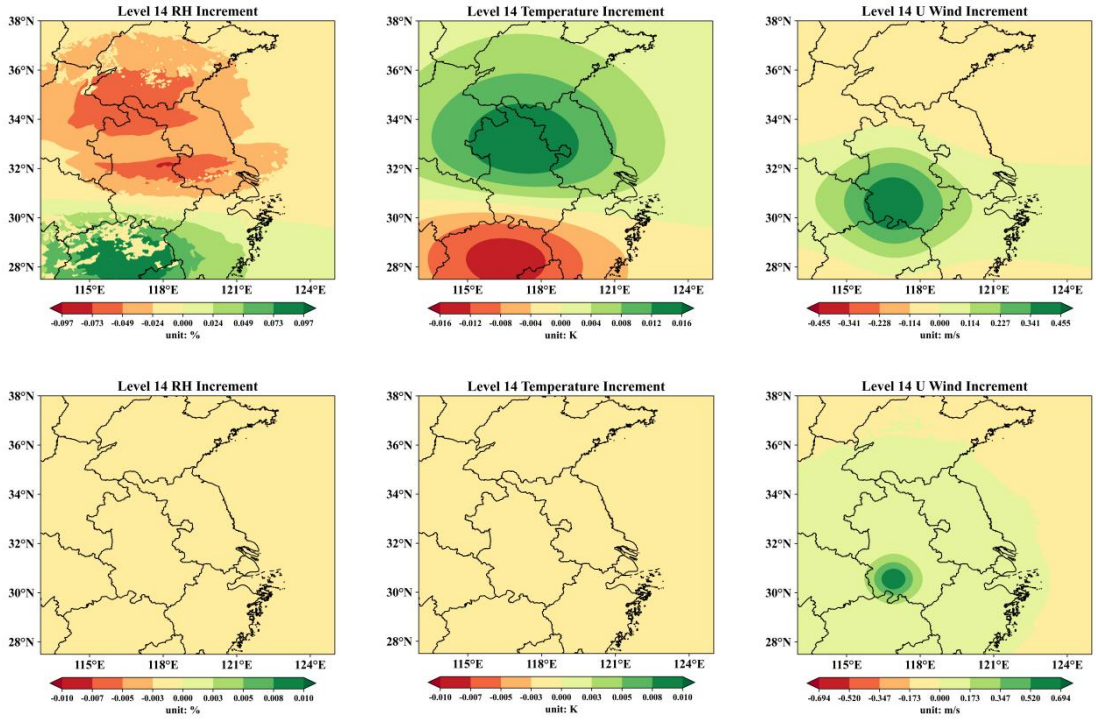

Figure 4-3. Analysis increments of relative humidity, temperature, and u-wind at level 14 under different control variable schemes in the single-observation experiment. The upper row corresponds to the CV5 scheme, and the lower row corresponds to the CV7 scheme.

4.3.2 Optimal Length-Scale Parameter

The horizontal length-scale parameter is a critical component of the background error covariance, as it determines the horizontal extent of analysis increments

generated by a single observation. If the length scale is set too large, analysis increments tend to be overly smooth, which can weaken localized strong signals. Conversely, an excessively small length scale may result in fragmented increment structures that lack spatial continuity. Therefore, achieving an appropriate balance between localization and continuity is essential for effective assimilation.

Sensitivity tests using multiple single-observation experiments reveal that the influence range of analysis increments contracts as the length-scale parameter decreases, making local structures more prominent. In contrast, increasing the length-scale parameter significantly expands the spatial coverage of the increments and leads to a smoother response structure. For the squall-line convective case investigated in this study, a length scale that is too large would fail to preserve the localized structural features of the wind and thermal fields. However, a length scale that is too small would cause increments to become too concentrated, hindering the formation of a continuous and physically consistent analysis field.

Based on a comprehensive analysis of the spatial extent of the increments, the ability to characterize local structures, and the consistency with the environmental features of severe convection, this study selected len_scaling=0.3 as the background error parameter for the formal assimilation experiments. This configuration, as illustrated in the resulting increment structures, ensures distinct localized response features while maintaining a reasonable level of spatial continuity. Consequently, it is deemed most suitable for the subsequent radar data assimilation experiments in this research.

Figure 4-4 displays the spatial distributions of u-wind, temperature, and moisture increments under the influence of a single observation. The analysis increments for all three variables are centered near the observation point and decay smoothly toward the surrounding regions, exhibiting regular spatial structures. These results indicate that the current background error covariance and control variable transforms effectively propagate local observational information to neighboring grid points while avoiding non-physical oscillations.

Regarding the response differences among variables, the u-wind increment

exhibits a relatively larger influence range, suggesting that momentum variables possess stronger spatial propagation characteristics under the constraints of the background error covariance. The distribution of the temperature increment is morphologically similar to that of the u-wind, but its magnitude is significantly smaller, indicating a milder response of thermal variables to a single observation. The moisture increment is the most concentrated and decays the fastest, reflecting the inherent localization of water vapor variables. These differences align with the physical characteristics of severe convective systems, where wind and temperature fields are often influenced by regional dynamics, whereas moisture perturbations remain concentrated near local convective trigger and maintenance zones.

Importantly, the increment distributions shown in Figure 4-4 exhibit high spatial continuity without isolated noise or anomalous long-distance diffusion. This confirms the reasonableness of the initial control variable parameter settings and establishes a robust foundation for further optimization in the subsequent stages of the study.

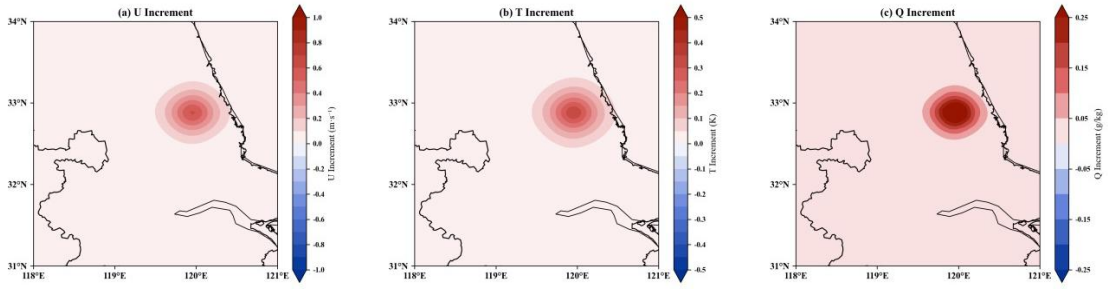

Figure 4-4. Analysis increments of u-wind, temperature, and humidity at level 10 under a single observation (len_scaling = 0.3, var_scaling = 2.0): (a) u-wind increment, (b) temperature increment, and (c) humidity increment.

4.4 Impact of Different Control Variable Schemes on Forecast Results

After identifying CV7 as the more suitable control-variable scheme for the subsequent formal data assimilation experiments, composite reflectivity forecasts were further compared to examine how different control-variable schemes affect the prediction of this severe convective case, particularly with respect to squall-line structure and echo evolution

Figure 4-5 presents the observed composite reflectivity and the corresponding

forecast results from the CV5 and CV7 schemes at 15:00, 16:00, and 17:00. Overall, both schemes are able to reproduce the main banded strong-echo structure over the study area, although noticeable differences from the observations remain. Under the CV5 scheme, the forecast echo coverage is relatively broader, and the localized intense echo centers appear more diffuse. In contrast, the CV7 scheme produces more concentrated intense echo centers and a more coherent banded organization, with localized convective cells and echo structures appearing more clearly defined.

In terms of temporal evolution, during 15:00–17:00, the CV7 scheme is generally closer to the observations than the CV5 scheme in reproducing the position, morphology, and localized intense echo centers of the main echo band. This advantage is particularly evident in the organization and development of localized convective structures. These results suggest that the CV7 control-variable scheme is more favorable for retaining localized dynamical information in the background error covariance, and that this advantage can be carried forward during model integration into a more realistic simulation of echo structure and hydrometeor distribution.

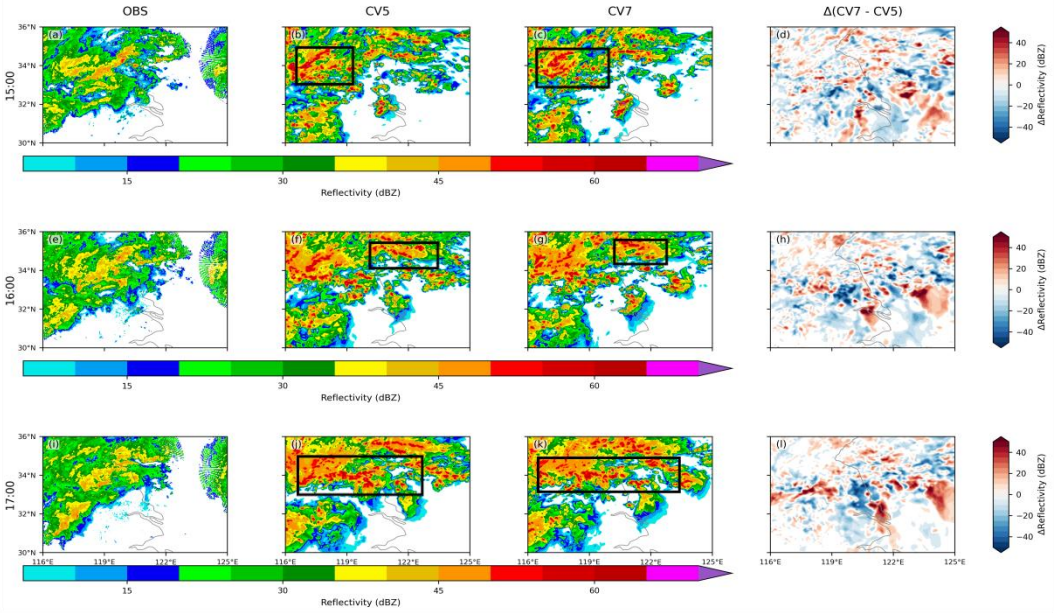

Figure 4-5. Radar reflectivity forecasts for 1–3 h initialized at 14:00 on 1 July 2024.

The composite reflectivity forecasts indicate that the choice of control-variable scheme has a clear influence on the prediction of this severe convective event. Although the CV5 scheme tends to produce relatively smooth and continuous analysis and forecast fields, its representation of localized mesoscale and convective-scale

structures is comparatively weak. By contrast, the CV7 scheme is more favorable for maintaining and developing localized dynamical features during severe convection and therefore provides a better overall representation of echo organization and localized intense echoes in this case. Accordingly, CV7 was selected as the control-variable scheme for the subsequent radar data assimilation experiments in this study.

4.5 Summary

This chapter investigated the impact of different control variable schemes on radar data assimilation and subsequent forecasting. First, the fundamental characteristics and differences between the CV5 and CV7 schemes in WRFDA were examined. CV5 utilizes the stream function and unbalanced velocity potential as momentum control variables, emphasizing the construction of analysis increments through statistical balance constraints. In contrast, CV7 directly employs horizontal wind components u and v as momentum control variables, which is more conducive to characterizing localized wind field structures.

Second, the spatial distribution characteristics of analysis increments under both schemes were compared through single-observation experiments. The results demonstrated that under identical length-scale conditions, the CV5 scheme produced broad responses in the temperature and humidity fields, accompanied by significant diffusion of wind field increments. Conversely, the CV7 scheme generated more localized and concentrated wind field increments, effectively preserving fine-scale details near the observation site. For the squall-line case investigated in this study, such localized response characteristics are more suitable for recovering low-level convergence and local dynamic structures.

Furthermore, background error parameters were refined through length-scale sensitivity experiments. Based on a comprehensive evaluation of increment spatial extent, continuity, and consistency with convective environmental features, len_scaling=0.3 was selected as the background error parameter for subsequent experiments.

Finally, the impact of different control variable schemes on hydrometeor and

composite reflectivity forecasts was evaluated. The results indicated that the CV7 scheme generally outperformed CV5 in simulating localized hydrometeor structures and intense echo centers, thereby better maintaining the organizational structure of mesoscale convective systems. In conclusion, this study adopts the CV7 scheme with len_scaling=0.3 for the formal radar data assimilation experiments. This configuration provides the necessary foundation for the comparative analysis of multi-band radar data assimilation presented in the following chapter.

5. Impacts of the Joint Assimilation of X-band Radar Data on the Squall-line Case

5.1 Analysis Increments

This chapter further investigates the influence of jointly assimilating X-band phased-array radar (XPAR) data on the analysis and forecast fields for the squall line event that occurred on July 1, 2024. By comparing the control experiment (CTL), the S-band radar data assimilation experiment (DA_S), and the joint S-band and X-band radar data assimilation experiment (DA_S_X), we systematically evaluate the added value of XPAR data for numerical weather prediction (NWP). The evaluation focuses on wind field structures, hydrometeor analysis increments, dynamical field forecasts, radar reflectivity simulations, and precipitation forecasts.

5.1.1 Impact on Wind Field Structure

To examine the impact of jointly assimilating X-band radar data on the wind-field structure of the squall-line case, this study compares the analyzed wind fields at the beginning of the cycling assimilation period (12:00) and at its end (14:00). The 925 hPa wind field at 12:00 is used to show the differences in the initial low-level environmental fields among the experiments before cycling assimilation begins. The 925 hPa and 850 hPa wind fields at 14:00 are then used to assess how the low-level and lower–midlevel dynamical structures are adjusted after two hours of cycling assimilation.

Figure 5-1 shows the analyzed 925 hPa wind fields at 12:00. At this stage, all experiments are still in the early phase of cycling assimilation. All three experiments

capture a low-level southerly background flow over the study region, together with localized wind-speed gradient features. Compared with the control experiment, DA_S shows some adjustment in localized wind-speed centers and wind-direction organization after assimilating S-band radar data. After the further assimilation of X-band radar data, DA_S_X produces a more refined correction to the local wind-field structure. However, at this stage, its overall impact is still mainly reflected in the initial adjustment of the low-level environmental field.

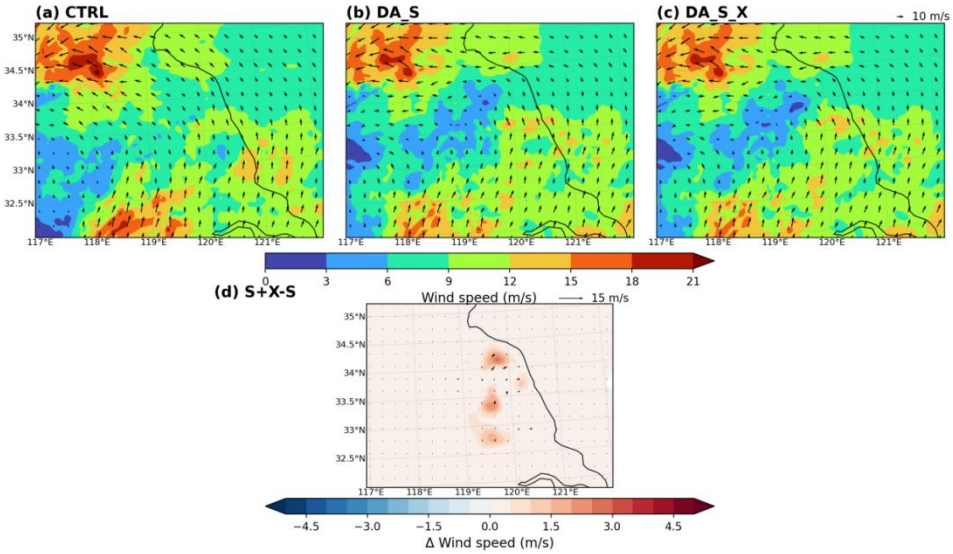

Figure 5-1. Comparison of the analyzed 925 hPa wind fields at 12:00 on 1 July 2024.

(a) CTRL, (b) DA_S, (c) DA_S_X, and (d) wind-speed differences between DA_S_X and DA_S. Shading denotes wind speed, and arrows denote horizontal wind vectors. In (d), shading denotes wind-speed differences, and arrows denote wind-field differences.

Figure 5-2 presents the analyzed 925 hPa wind fields at 14:00. After two hours of cycling assimilation from 12:00 to 14:00, the differences among the experiments become much more pronounced. Overall, all three experiments reproduce the low-level southerly background flow and the localized wind-speed distribution over the study region, but they differ substantially in the wind-field structure near the severe convective region.

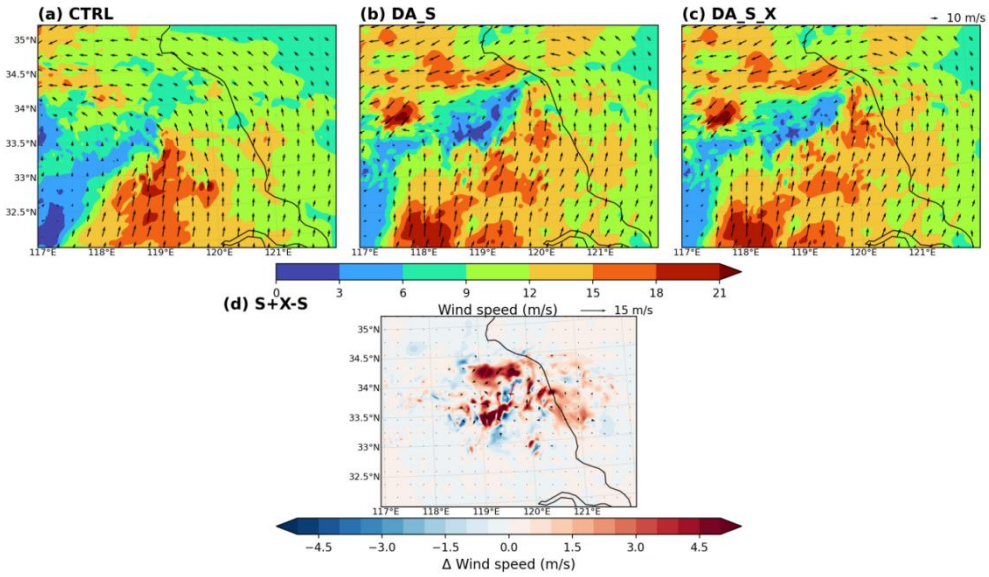

Figure 5-2. Comparison of the analyzed 925 hPa wind fields at 14:00 on 1 July 2024.

(a) CTRL, (b) DA_S, (c) DA_S_X, and (d) wind-speed differences between DA_S_X and DA_S. Shading denotes wind speed, and arrows denote horizontal wind vectors. In (d), shading denotes wind-speed differences, and wind-direction difference.

After the further joint assimilation of X-band radar data on top of DA_S, DA_S_X shows a more pronounced adjustment of the 925 hPa wind field. It can be seen that DA_S_X produces clearer localized wind-speed maxima and a more distinct wind-convergence structure near the convective band. This is especially evident over the area around 119°E–120°E and 33°N–34.5°N, where the wind-field pattern exhibits more pronounced mesoscale and convective-scale characteristics than that in DA_S. The difference field (DA_S_X − DA_S) further indicates that the additional impact of the X-band data is mainly concentrated in and around the region of severe convective activity, rather than being uniformly distributed across the entire study area. This suggests that the correction to the low-level wind field introduced by X-band radar data is strongly localized and can further enhance the representation of local convergence and wind-speed gradient structures.

Figure 5-3 presents the analyzed 850 hPa wind fields at 14:00. Overall, the three experiments maintain a generally consistent large-scale environmental wind pattern at 850 hPa, indicating that radar data assimilation does not alter the basic midlevel circulation over the study region. However, clear differences still appear near the area

of severe convective activity. Compared with CTRL, DA_S adjusts the location of the wind-speed maxima and the local wind-direction structure near the convective band extending from the central to northern part of the study region, making the correspondence between the lower–midlevel wind field and the convective-system distribution clearer. After the further assimilation of X-band radar data, DA_S_X still shows an additional correction to the 850 hPa wind field. Compared with that at 925 hPa, the spatial extent and intensity of this correction are reduced. Nevertheless, localized wind-speed differences and wind-direction adjustments remain evident near the convective band, indicating that the impact of the X-band data is concentrated mainly in the lower levels. Although this influence extends upward to 850 hPa, its magnitude becomes relatively weaker.

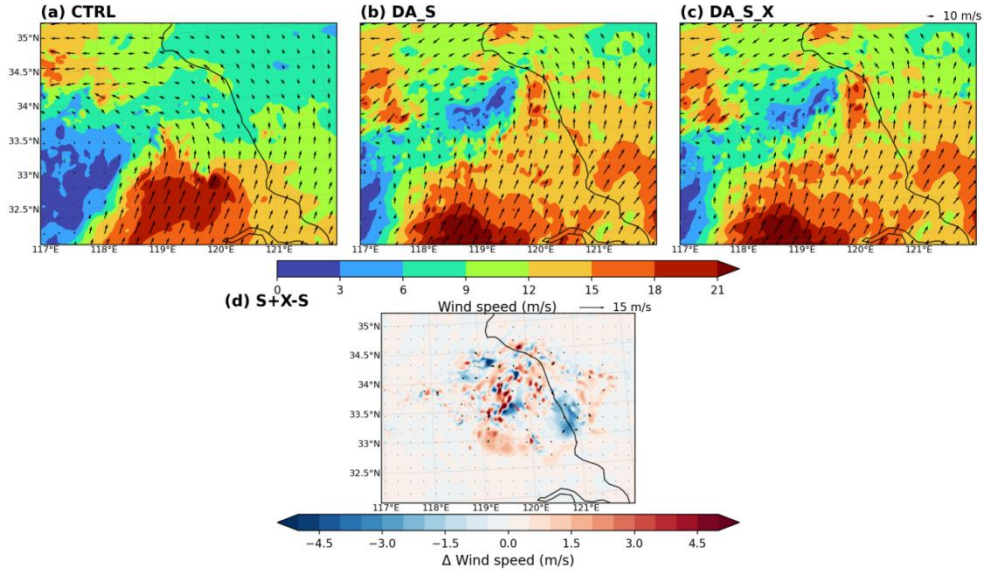

Figure 5-3. Comparison of the analyzed 850hPa wind fields at 14:00 on 1 July 2024.

(a) CTRL, (b) DA_S, (c) DA_S_X, and (d) wind-speed differences between DA_S_X and DA_S. Shading denotes wind speed, and arrows denote horizontal wind vectors. In (d), shading denotes wind-speed differences, and arrows denote wind-field differences.

In summary, comparing the results at 12:00 UTC and 14:00 UTC across the 925 hPa and 850 hPa levels reveals that the impact of radar data assimilation on the wind field evolves temporally and varies vertically. Localized adjustments to the low-level wind field strengthen as the cycling assimilation progresses. Specifically, XPAR data provides the most significant corrections to the near-surface and low-level structures.

While its influence at 850 hPa is more a supplementary adjustment of mesoscale structures rather than a change to the background circulation, the vertical decay of these corrections is physically consistent. This highlights the direct role of X-band data in improving low-level dynamical conditions and enhancing the characterization of localized convergence structures for squall line events.

5.1.2 Hydrometeor Analysis Increments

Figure 5-4 illustrates the spatial distributions of analysis increments (Analysis minus First Guess, AN − FG) for primary hydrometeors across various altitudes at 14:00 UTC on 1 July 2024, comparing the DA_S and DA_S_X experiments along with the incremental differences (DA_S_X minus DA_S). The rows from top to bottom represent analysis increments for the low-level rainwater mixing ratio, mid-level graupel mixing ratio, and high-level snow mixing ratio, respectively. This figure is used to evaluate the additional corrective effects of jointly assimilating X-band phased-array radar (XPAR) data on the microphysical structure of the severe convective system.

Regarding the low-level rainwater mixing ratio increments, both DA_S and DA_S_X exhibit distinct positive and negative increment distributions near the primary convective echo bands. This indicates that radar data assimilation exerts the most significant adjustment on low-level liquid hydrometeors. The regions with high increment values in both experiments are primarily aligned with the convective bands and localized strong echo centers, and their spatial positions are generally consistent. This suggests that S-band radar data can effectively correct the low-level rainwater structure within the main precipitation systems. Building upon this, the difference field (DA_S_X minus DA_S) further reveals that the joint introduction of XPAR data leads to additional adjustments in the low-level rainwater mixing ratio near localized strong echo regions. However, these impacts are primarily concentrated within the convective bands and near localized echo centers rather than being broadly distributed across the entire domain. This demonstrates that the influence of X-band data on the low-level rainwater field is characterized by high localization and fine-scale refinement.

Regarding the mid-level graupel mixing ratio increments, both DA_S and DA_S_X display relatively scattered yet concentrated positive and negative increment centers, primarily distributed near the northern main convective band and localized intense convective cells. Compared to the rainwater mixing ratio, the graupel mixing ratio increments exhibit smaller spatial scales and stronger localization. This indicates that microphysical processes related to graupel particles are more sensitive to localized strong updrafts and intense echo cores. The difference field shows that the additional impact of X-band radar data on the graupel mixing ratio is generally weaker than its impact on rainwater. However, clear corrective signals are still visible near localized intense convective centers. This suggests that the joint assimilation of X-band data improves the representation of mid-level ice-phase and mixed-phase particles, though this influence is mainly confined to regions corresponding to localized strong echoes.

Regarding the high-level snow mixing ratio increments, both experiments generate prominent positive and negative increment centers at high altitudes, primarily located above the main convective band and in the rear regions of the convective system. Overall, the distribution patterns of the snow mixing ratio increments in DA_S and DA_S_X are quite similar. This indicates that the adjustment of the high-level ice-phase particle field is still dominated by the information provided by S-band radar data assimilation. Meanwhile, the difference field (DA_S_X minus DA_S) reveals that although some differences exist in the high-level snow mixing ratio in certain localized areas after joint assimilation, the overall magnitude is small and the spatial distribution is more dispersed. This suggests that the direct impact of X-band data on the high-level ice-phase particle field is relatively limited. Its primary role remains the supplementary correction of microphysical structures in the lower and middle levels of the convective system.

Synthesizing the results of the three types of hydrometeor analysis increments reveals that the adjustments exhibit distinct hierarchical characteristics. The response is strongest for the low-level rainwater mixing ratio, followed by the mid-level graupel mixing ratio, and is relatively weak for the high-level snow mixing ratio.

Compared to assimilating S-band radar data alone, the joint assimilation of XPAR data provides additional incremental impacts primarily within the convective bands and near localized strong echo centers. This is manifested as refined localized corrections for low-level liquid hydrometeors and mid-level mixed-phase particles, rather than a large-scale reconstruction of the entire hydrometeor field. These findings are consistent with the superior capability of X-band phased-array radar to detect fine-scale structures at low levels and its higher sensitivity to localized mesoscale and small-scale severe convective systems.

Consequently, the analysis of hydrometeor increments indicates that the joint assimilation of XPAR data can further improve the localized representation of microphysical structures within severe convective systems. The adjustments are particularly pronounced for the distribution of low-level precipitation particles and hydrometeors near localized strong echo cores. Such supplementary corrections to the microphysical analysis fields are conducive to enhancing the accuracy of subsequent echo forecasts and short-duration heavy rainfall predictions.

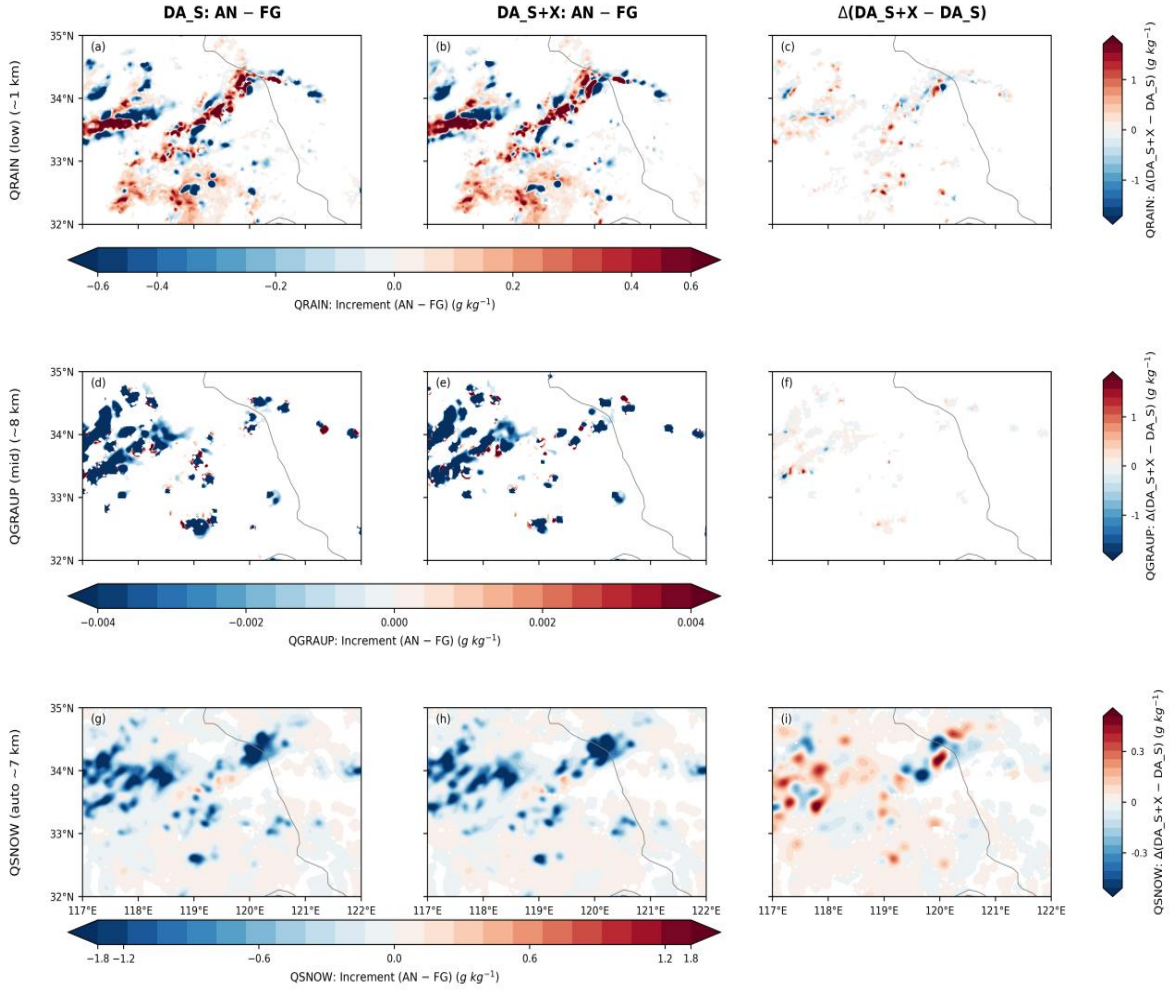

Figure 5-4. Comparison of the analysis increments (AN − FG) of the major hydrometeors in different experiments at 14:00 UTC on 1 July 2024.

The first row shows the increment of rainwater mixing ratio in the lower levels, the second row shows the increment of graupel mixing ratio in the middle levels, and the third row shows the increment of snow mixing ratio in the upper levels. The left, middle, and right columns represent DA_S, DA_S_X, and DA_S_X−DA_S, respectively. This figure is used to compare the additional impacts of jointly assimilating X-band phased-array radar data on the hydrometeor analysis fields at different heights.

5.2 Forecast Results

5.2.1 Dynamical Field Forecasts

To further assess the impact of jointly assimilating X-band phased-array radar

(XPAR) data on the dynamical field forecasts of the squall line case, this study compares the 925 hPa wind field and the 850 hPa divergence-wind field forecasts during the period from 15:00 to 17:00 UTC. Figure 5-5 illustrates the wind speed and horizontal wind vector distributions for the different experiments at the 925 hPa level, while Figure 5-6 displays the 850 hPa divergence fields overlaid with wind vectors.

Regarding the 925 hPa wind field forecasts, all three experiments effectively maintain the low-level southerly background flow and capture localized wind speed variations near the convective active regions. However, notable differences exist in their ability to simulate fine-scale wind field structures. The overall wind field in the CTL experiment appears excessively smooth, with a relatively weak representation of localized velocity centers, wind speed gradients, and low-level directional adjustments. In contrast, the DA_S experiment enhances the velocity centers near the convective zones across multiple time steps and clarifies the spatial alignment between the localized wind structures and the convective bands. This demonstrates that the assimilation of S-band radar data exerts a positive influence on low-level dynamical field forecasts.

The integration of XPAR data in the DA_S_X experiment further improves the performance of the 925 hPa wind field forecasts. Between 15:00 and 17:00 UTC, DA_S_X generally outperforms DA_S in characterizing high-velocity bands, wind speed gradients, and the organizational structure of the wind field. This improvement is particularly evident in the region between 119°E–120°E and 33°N–34.5°N, where the wind field structures more accurately reflect the mesoscale and small-scale environmental changes surrounding the severe convective system. Compared to DA_S, the local wind speed distribution in DA_S_X exhibits greater structural complexity, and the wind vector adjustments near the convective regions are more distinct. These results indicate that XPAR data provides enhanced refinement of local details within low-level wind field forecasts.

The 850 hPa divergence and wind field forecasts show that while all three experiments reproduce the fundamental environmental flow and the general convergence-divergence patterns, substantial disparities emerge in the simulation of

localized divergence structures and convective organization. In the CTL experiment, although the divergence field exhibits a banded structure roughly aligned with the convection, the convergence and divergence centers remain fragmented and poorly organized. The DA_S experiment improves upon this by enhancing the continuity of the divergence bands and clarifying the localized convergence-divergence configurations, indicating that S-band radar data assimilation significantly refines the mid-to-low level dynamical adjustments.

Furthermore, the joint assimilation of XPAR data in DA_S_X produces even clearer and more continuous banded features in the 850 hPa divergence field. Compared to DA_S, DA_S_X establishes stronger localized convergence-divergence configurations near the convective bands, featuring superior organization and better spatial correspondence between the divergence centers and the active convective zones. This is particularly noticeable at 16:00 and 17:00 UTC, where DA_S_X’s characterization of the divergence structures near the main convective band is significantly better than both CTL and DA_S. This suggests that X-band data not only improves low-level wind speed distributions but also enhances the refined characterization of mid-to-low level divergence structures. Such improvements are critical for squall line systems, as their development and maintenance are highly dependent on mid-to-low level convergence, updraft intensity, and their interaction with the ambient wind field.

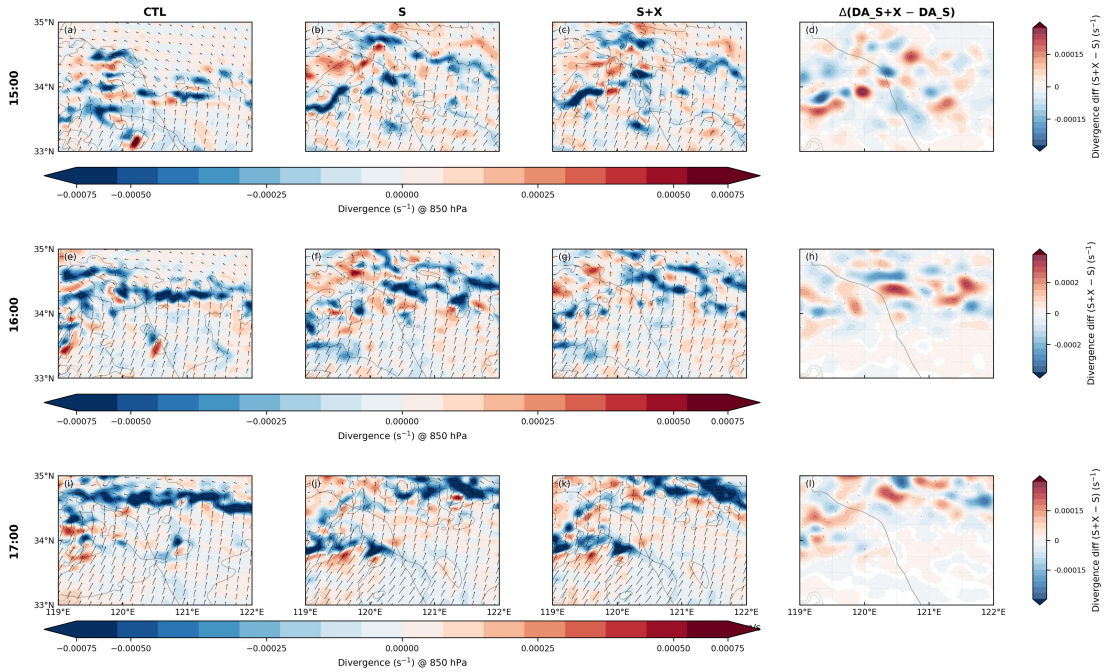

Figure 5-5. Comparison of the forecast 850 hPa divergence and wind fields in different experiments at 15:00, 16:00, and 17:00 on 1 July 2024.

The three rows correspond to 15:00, 16:00, and 17:00, respectively, and the three columns represent CTL, DA_S, and DA_S_X. Shading denotes divergence, and arrows denote horizontal wind vectors. This figure is used to compare the impacts of jointly assimilating X-band phased-array radar data on the forecast convergence–divergence structure and wind field in the lower and middle levels.

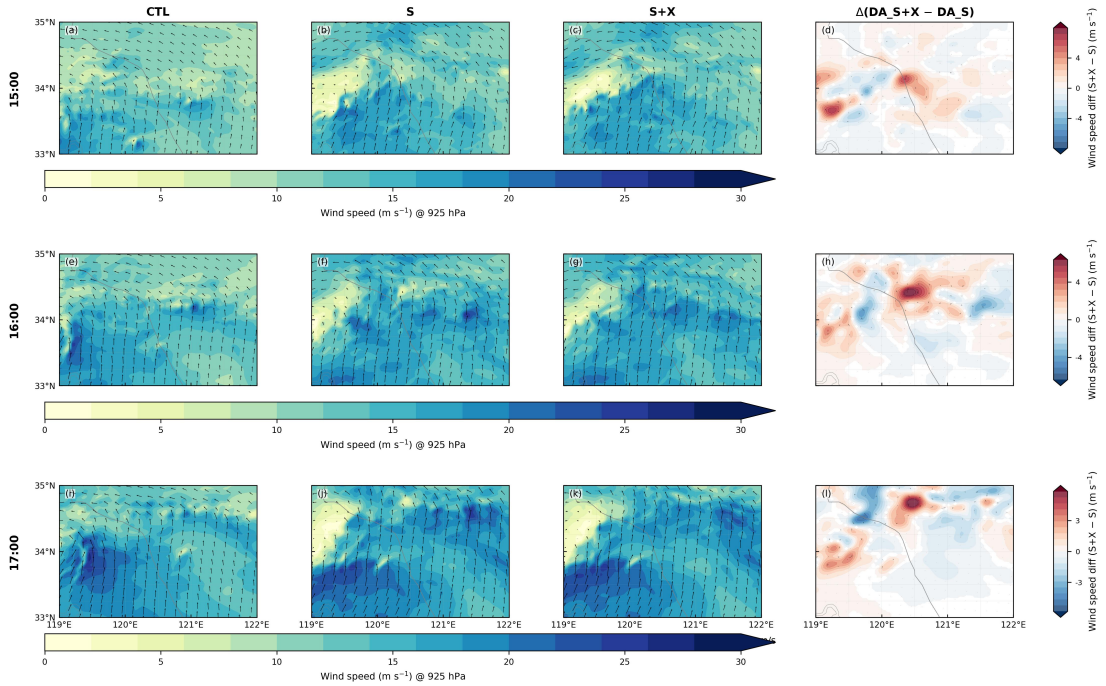

Figure 5-6.Comparison of the forecast 925 hPa wind fields in different experiments at 15:00, 16:00, and 17:00 on 1 July 2024.

The three rows correspond to 15:00, 16:00, and 17:00, respectively, and the three columns represent CTL, DA_S, and DA_S_X. Shading denotes wind speed, and arrows denote horizontal wind vectors. This figure is used to compare the impacts of jointly assimilating X-band phased-array radar data on the forecast structure of the low-level wind field.

A synthesis of the 925 hPa wind field and 850 hPa divergence-wind field forecast results indicates that the improvements in dynamical field forecasts through radar data assimilation exhibit distinct hierarchical and persistent characteristics. While the CTL experiment provides only a coarse representation of the environmental background, the DA_S experiment yields improvements in both the low-level wind field and the mid-to-low-level divergence structures. Building upon these enhancements, the DA_S_X experiment further strengthens the representation of localized wind speed centers, velocity gradients, convergence zones, and divergence structures, thereby aligning the dynamical field forecasts more closely with the meso-and-microscale organizational features of severe convective systems. These findings suggest that X-band phased-array radar data plays a constructive role in

refining the dynamical structure forecasts for squall-line convective events.

5.2.2 Radar Reflectivity Forecasts

To evaluate the impact of different radar data assimilation schemes on the reflectivity forecasts of the squall line case, this study presents a comparative analysis focusing on both the spatial distribution of composite reflectivity and the corresponding verification scores. Figure 5-7 displays the observed composite reflectivity alongside the forecast results from the CTRL, DA_S, and DA_S_X experiments at 15:00, 16:00, and 17:00 UTC. Additionally, Figure 5-8 illustrates the temporal evolution of the echo BIAS for these experiments at the 20 dBZ and 40 dBZ thresholds.

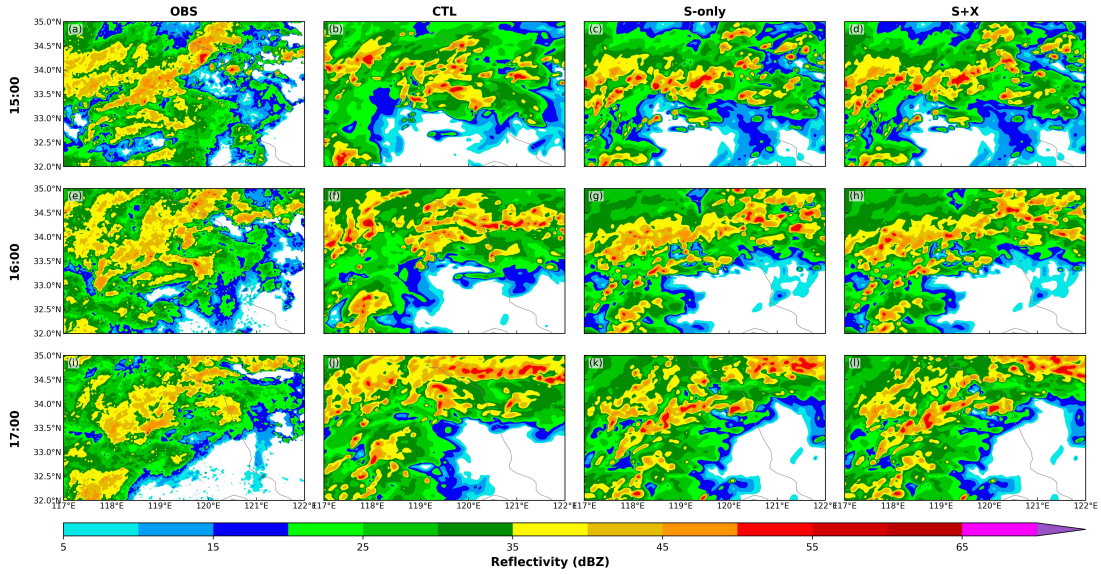

Figure 5-7. Comparison of the observed and forecast composite reflectivity in different experiments at 15:00, 16:00, and 17:00 on 1 July 2024.

The four columns represent OBS, CTRL, DA_S, and DA_S_X, respectively, and the three rows correspond to 15:00, 16:00, and 17:00. The red boxes indicate regions with more pronounced local differences. This figure is used to compare the impacts of jointly assimilating X-band phased-array radar data on the structure of the echo band and the simulation of local intense echo centers.

Regarding the spatial distribution of composite reflectivity, the observed reflectivity fields exhibit a continuous band-like structure with multiple strong echo

centers embedded within, which reflects the high degree of organization and distinct mesoscale structural features characteristic of squall line systems. Although the CTRL experiment successfully simulates the position and general orientation of the main echo band within the study domain, it shows lower continuity in the echo band compared to the observations. Furthermore, CTRL fails to accurately capture the localized strong echo centers, particularly in the central and eastern segments of the convective band, where the echo structure appears fragmented. The simulation of embedded strong echo cores is also notably weak in this experiment. These results indicate that the model possesses a limited capability to represent the fine-scale internal structures of severe convective systems when radar data is not assimilated.

The inclusion of S-band radar data in the DA_S experiment leads to a marked improvement in composite reflectivity forecasts relative to the CTRL run. During the 15:00 – 17:00 UTC period, DA_S effectively captures the continuous nature of the main echo band and enhances the simulation of localized strong echo centers. This improvement is particularly evident in the region highlighted by the red box in Figure 5-7, where DA_S successfully reproduces the banded structure and embedded intense cores seen in the observations. These findings demonstrate that S-band radar data assimilation effectively refines the overall echo distribution and organizational morphology of the convective system.

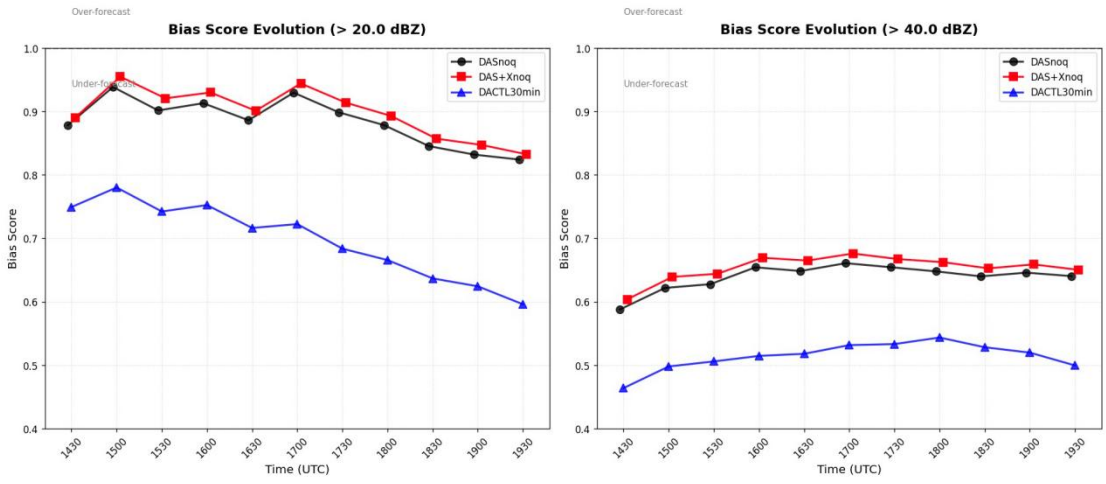

Figure 5-8. Temporal evolution of echo BIAS under the 20 dBZ and 40 dBZ thresholds in different

experiments.

The left panel corresponds to the 20 dBZ threshold, and the right panel corresponds to the 40 dBZ threshold. The black, red, and blue lines denote DA_S, DA_S_X, and CTRL, respectively. This figure quantitatively compares the forecast biases of different experiments in the coverage of moderate and strong echoes.

The reflectivity forecast is further optimized in the DA_S_X experiment, which incorporates X-band phased-array radar data alongside the S-band data. Compared to DA_S, the DA_S_X experiment consistently yields clearer echo band structures and more accurate distributions of localized strong echo centers across multiple time steps. In the key area indicated by the red box, DA_S_X provides a superior simulation of the positions and shapes of the intense echo cores, as well as the internal details of the banded structure. At certain times, DA_S_X also exhibits better echo continuity and a stronger capability to characterize localized structures compared to DA_S. This confirms that the addition of X-band phased-array radar data further enhances the model's ability to simulate the fine-scale reflectivity structures of severe convective systems.

In terms of temporal evolution, all three experiments maintain the basic orientation of the main echo band between 15:00 and 17:00 UTC. However, the CTRL experiment consistently shows lower levels of local organization and weaker representation of intense echo cores. While DA_S shows significant improvements, DA_S_X further refines the localized strong echo centers and the internal structural details of the convective band at various time steps. This suggests that the benefits of jointly assimilating X-band radar data are not confined to the analysis time but persist throughout the short-term forecast period following the model integration.

Figure 5-8 presents the temporal variations in echo BIAS for the different experiments at the 20 dBZ and 40 dBZ thresholds. The BIAS values for all three experiments remain below 1.0 at both thresholds, indicating a general tendency toward underestimation; however, clear differences exist between the schemes. At the 20 dBZ threshold, the BIAS values for DA_S and DA_S_X are significantly higher than those of CTRL and are closer to the ideal value of 1.0. This indicates that radar

data assimilation substantially improves the forecast of medium-intensity echo coverage. Notably, DA_S_X yields slightly higher BIAS values than DA_S at most time steps, suggesting that the joint assimilation of X-band data brings the simulated extent of echoes above 20 dBZ closer to the observed levels.

At the 40 dBZ threshold, the BIAS values for all experiments are generally lower than those at the 20 dBZ threshold, which reflects a persistent underestimation of strong echo regions. Nevertheless, both DA_S and DA_S_X show significant improvements over CTRL. The DA_S_X experiment consistently maintains the highest BIAS values throughout the period, demonstrating that the joint assimilation of X-band phased-array radar data further improves the simulation of strong echo core coverage. Although some underestimation remains at the 40 dBZ threshold for all experiments, the performance gain of DA_S_X relative to CTRL and DA_S is robust and stable.

In summary, the comprehensive analysis of composite reflectivity distributions and echo BIAS scores confirms that radar data assimilation significantly enhances squall line reflectivity forecasts. S-band radar data assimilation provides fundamental improvements in the continuity and organizational structure of the echo band. Building on this, the further introduction of X-band phased-array radar data strengthens the model's ability to simulate localized intense cores and refined internal structures, bringing the forecasted echo coverage into closer agreement with observations. Thus, the joint assimilation of X-band phased-array radar data plays a positive role in improving the quality of reflectivity forecasts for severe convective weather.

5.2.3 Precipitation Forecasts

To further evaluate the impact of jointly assimilating X-band phased-array radar (XPAR) data on short-duration heavy precipitation forecasts, this study analyzes the hourly precipitation through both spatial distribution and quantitative verification scores. Figure 5-9 presents the observed hourly precipitation alongside the forecast results from the different experiments at 15:00, 16:00, and 17:00 UTC.Additionally,

Figures 5-10 and 5-11 illustrate the temporal evolution of the 1-h precipitation BIAS and FSS scores at the 5 mm and 10 mm thresholds.

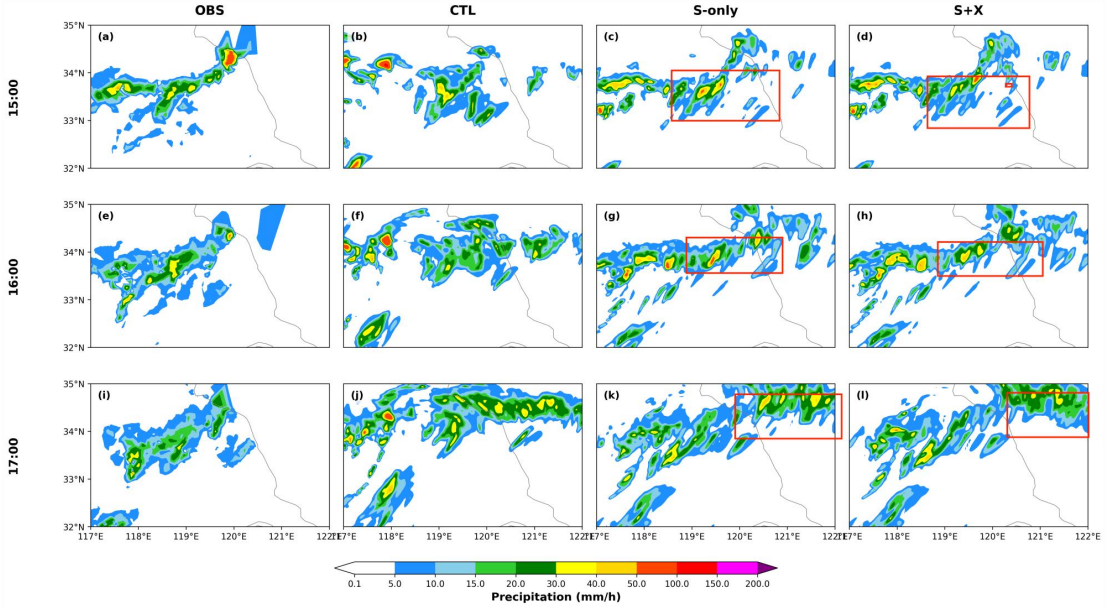

Figure 5-9.Comparison of the observed hourly precipitation and the 1–3 h accumulated precipitation forecasts initialized at 14:00 UTC on 1 July 2024 for 15:00–17:00.

The four columns represent OBS, CTRL, DA_S, and DA_S_X, respectively, and the three rows correspond to 15:00, 16:00, and 17:00. The red boxes indicate regions with more pronounced local differences.

From the perspective of hourly spatial distribution, the observed precipitation is characterized by a banded structure with a southwest-to-northeast orientation. This structure contains localized intense precipitation centers, which is a typical feature of squall-line-type severe convective precipitation. Although the CTRL experiment roughly simulates the positions of the main precipitation bands, the simulated precipitation field is relatively fragmented and the local rain bands exhibit poor continuity. Furthermore, CTRL suffers from significant precipitation center position errors and an over-expansion of the strong precipitation areas across multiple time steps. Notably, at 16:00 and 17:00 UTC, the CTRL experiment provides an insufficient characterization of the localized intense precipitation cores within the main band while producing spurious precipitation bands in several regions. These results indicate that the model's ability to simulate meso-and-microscale precipitation structures is limited without the assimilation of radar data.

The DA_S experiment shows significant improvements in hourly precipitation forecasts compared to the CTRL run following the assimilation of S-band radar data. Between 15:00 and 17:00 UTC, DA_S effectively recovers the continuity and spatial organization of the main precipitation bands. The correspondence between the simulated intense precipitation centers and the observations also improves. Specifically, in the area highlighted by the red box in Figure 5-9, the DA_S experiment successfully reproduces the banded precipitation structure and the embedded intense cores seen in the observations. This confirms that S-band radar data assimilation plays a constructive role in correcting the position and morphology of precipitation bands.

Precipitation forecast results are further optimized in the DA_S_X experiment, which incorporates XPAR data on top of the S-band data. Compared to DA_S, the DA_S_X experiment provides a more realistic representation of the internal details and localized intense centers of the main precipitation band at various time steps. Within the red-boxed region, the simulation of the center positions, intensities, and organizational structures of the precipitation bands in DA_S_X aligns more closely with the observations. At 16:00 and 17:00 UTC, DA_S_X demonstrates superior performance in maintaining precipitation continuity in the middle and eastern segments of the main band, and the distribution of localized high-value precipitation areas is more consistent with observed features. These findings suggest that the inclusion of XPAR data further enhances the model's capability to simulate localized meso-and-microscale precipitation structures.

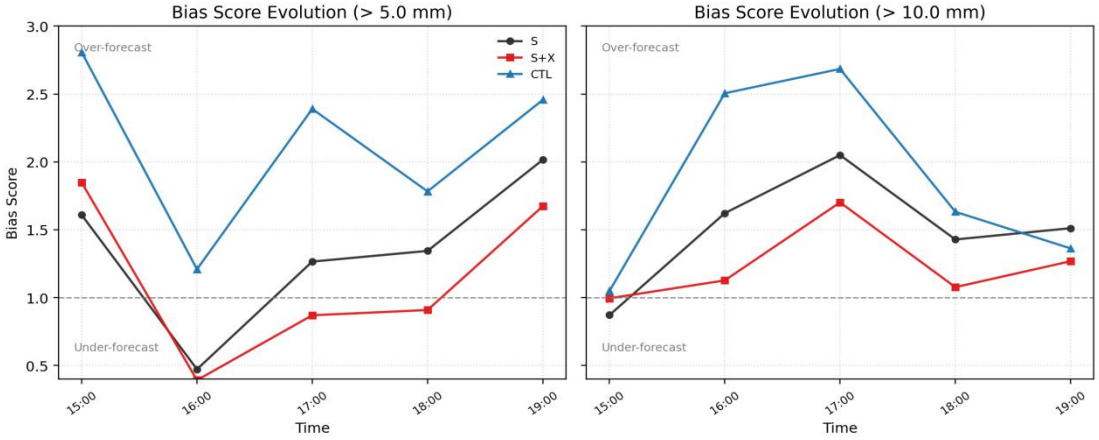

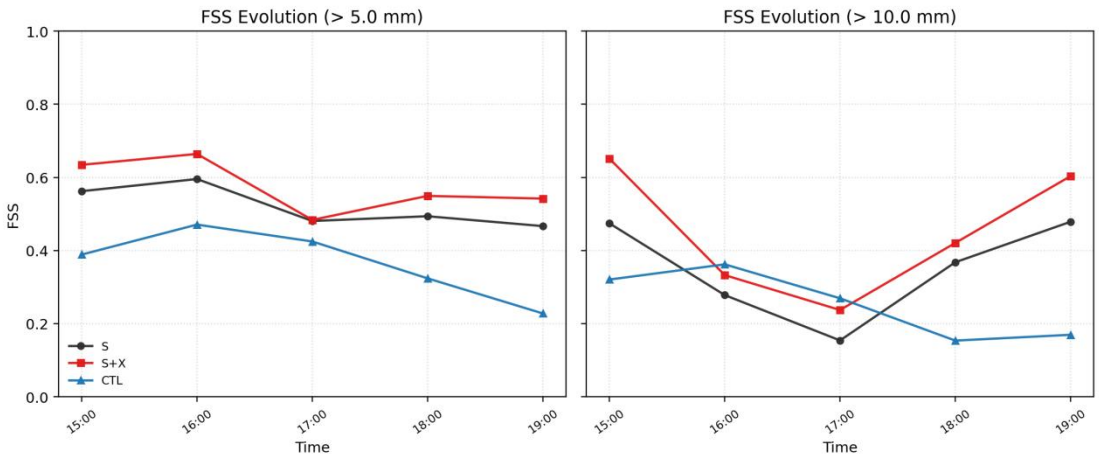

Figure 5-10. Temporal evolution of 1 h precipitation BIAS and FSS scores under the 5 mm and 10 mm thresholds in different experiments (FSS radius: 15 km).

Regarding the BIAS scores at the 5 mm threshold, the CTRL experiment consistently yields values significantly greater than 1.0, which reflects an overestimation of the medium-intensity precipitation area. The DA_S scores are generally closer to the ideal value than those of CTRL, while the DA_S_X scores remain closest to 1.0 across most time steps. This demonstrates that the joint assimilation of XPAR data further reduces the forecast bias for precipitation coverage above 5 mm. At the 10 mm threshold, the CTRL experiment maintains a pronounced high bias, whereas the scores for DA_S and DA_S_X remain more stable. Among these, DA_S_X provides the most reasonable characterization of the heavy precipitation coverage.

The FSS scores generally increase as the neighborhood scale expands, which indicates the presence of certain spatial displacement errors in the precipitation forecasts. At the 5 mm threshold, both DA_S and DA_S_X achieve significantly higher FSS values than the CTRL experiment. DA_S_X consistently attains the highest scores across most time steps and neighborhood scales, demonstrating its superior performance in simulating the spatial distribution of medium-intensity precipitation. At the 10 mm threshold, although the FSS values for all experiments are lower than those at the 5 mm threshold—reflecting the increased difficulty in forecasting heavy rainfall—the disparities between the experiments remain distinct. Both DA_S and DA_S_X outperform CTRL, and DA_S_X maintains the highest FSS

values overall. This reflects its stronger capability to simulate localized heavy precipitation centers and their corresponding spatial extents.

In conclusion, the synthesized BIAS and FSS results confirm that the joint assimilation of XPAR data not only reduces the bias in hourly precipitation coverage but also enhances the spatial consistency between the forecasts and observations. While S-band radar data assimilation significantly improves the simulation of the positions and continuity of precipitation bands, the further introduction of X-band data refines the banded structures, localized intense centers, and spatial matching degree. These results indicate that the joint assimilation of X-band phased-array radar data is highly effective for improving the quality of short-duration heavy precipitation forecasts during severe convective events.

5.3 Summary

Building upon the optimal control variable scheme and background error parameters established in Chapter 4, this chapter systematically evaluates the impact of jointly assimilating X-band phased-array radar (XPAR) data on the analysis and forecast fields for the squall line case of 1 July 2024. By comparing the control experiment (CTL), the S-band radar data assimilation experiment (DA_S), and the joint S-band and X-band radar data assimilation experiment (DA_S_X), we assess the added value of XPAR data across several dimensions, including wind field structures, hydrometeor analysis increments, dynamical field forecasts, radar reflectivity simulations, and precipitation forecasts.

The analysis field results demonstrate that the joint assimilation of XPAR data further refines both the low-level wind field and the hydrometeor field. Regarding the wind field, the corrective impact of X-band data on the 925 hPa structure becomes increasingly significant as cycling assimilation progresses, resulting in clearer localized wind speed maxima and directional convergence structures near active convective regions. While this influence extends upward to 850 hPa, its magnitude decays with height, confirming that X-band data provides more direct improvements to near-surface dynamical conditions. Regarding hydrometeors, the additional adjustments from X-band data are primarily concentrated within convective bands and

near localized strong echo centers. These adjustments are manifested as refined localized corrections to the low-level rainwater mixing ratio and mid-level graupel mixing ratio, whereas the direct impact on the high-level snow mixing ratio is relatively limited. These findings indicate that XPAR data effectively supplements S-band observations to improve the localized characterization of microphysical structures within severe convective systems.

The forecast results indicate that the joint assimilation of XPAR data exerts a positive influence on the dynamical, reflectivity, and precipitation field forecasts for this squall line event. In terms of dynamical field forecasts, the DA_S_X experiment produces clearer localized wind speed gradients and convergence-divergence configurations at both 925 hPa and 850 hPa, reflecting more realistic meso-and-microscale organizational features. This suggests that X-band data enhances the model's ability to simulate the dynamical structures of the lower and middle atmosphere. Regarding radar reflectivity forecasts, DA_S_X outperforms both CTL and DA_S in representing the continuity of the main echo band, the positions of localized intense cores, and internal structural details. Furthermore, the echo BIAS scores confirm that incorporating X-band data brings the forecasted coverage of reflectivity above 20 dBZ and 40 dBZ into closer agreement with observations. In terms of precipitation forecasts, DA_S_X provides the most reasonable characterization of banded rainfall structures and localized heavy precipitation centers, consistently achieving superior spatial distributions and quantitative scores. The BIAS results show a reduction in coverage errors, while the FSS results demonstrate an enhanced capability to match the spatial locations of medium-to-heavy precipitation zones.

In conclusion, further introducing X-band phased-array radar data on the basis of S-band radar assimilation more effectively improves the analysis and forecasting of squall-line-type severe convective systems. Its primary advantages lie in the refined characterization of low-level wind fields, local microphysical features, intense echo centers, and short-duration heavy rainfall regions. These results highlight the significant application potential of XPAR data in numerical weather prediction and

demonstrate that multi-band joint assimilation provides robust observational support for enhancing short-term forecasting of severe convective weather.

6. Summary and Outlook

This study investigates a squall-line severe convective event that occurred over the middle and lower reaches of the Yangtze River on 1 July 2024. Based on the WRF model and its WRFDA 3DVar assimilation system, a series of multi-band weather radar data assimilation experiments were conducted. Particular attention was given to the effects of assimilating S-band radar data alone and jointly assimilating S-band and X-band radar data on the analysis and forecast fields of this severe convective case. On this basis, the effects of control-variable schemes, background error covariance parameters, and joint assimilation of multi-band radar data were systematically examined. The main conclusions are as follows.

6.1 Main Conclusions

(1) CV7 is more suitable than CV5 for radar data assimilation in this squall-line severe convective case.

Idealized single-observation experiments show that, under the same length-scale settings, the CV5 scheme tends to produce analysis increments with broader spatial extent and stronger smoothness, and the observational information is more readily spread into the temperature and moisture fields. In contrast, the CV7 scheme responds more directly to wind-field structure and generates analysis increments that are more localized and concentrated. It is therefore more favorable for preserving the mesoscale and convective-scale dynamical structures of severe convection. Sensitivity experiments further show that the horizontal correlation length scale of background error covariance strongly affects the spatial extent and continuity of the analysis increments. When the length scale is too large, the increments become overly smooth and localized strong signals are weakened. When it is too small, the increments become overly concentrated, making it difficult to obtain a continuous and physically reasonable analysis field. Based on a comprehensive assessment of the locality and continuity of the analysis increments and their consistency with the environmental characteristics of severe convection, this study selected CV7 as the control-variable

scheme and identified len_scaling = 0.3 as the optimal parameter setting.

(2) The joint assimilation of X-band radar data further improves the analysis fields of the severe convective case.

On the basis of assimilating S-band radar data, the further incorporation of X-band radar data leads to more refined corrections in both the low-level wind field and the hydrometeor field. This result indicates that X-band radar observations can provide additional useful information for improving the analysis of severe convective systems, particularly in terms of low-level dynamical structure and hydrometeor distribution.

(3) The joint assimilation of X-band radar data improves short-term heavy-rainfall forecasts.

The hourly precipitation forecasts show that CTRL produces a fragmented simulation of the main precipitation band, with relatively large errors in the locations of localized heavy-rainfall centers. DA_S clearly improves the continuity and banded structure of the precipitation zone. On this basis, DA_S_X further enhances the simulation of localized heavy-rainfall centers, banded precipitation structure, and the distribution of heavy-rainfall areas. The BIAS and FSS results indicate that DA_S_X performs best under both the 5 mm and 10 mm thresholds. This suggests that the joint assimilation of X-band radar data improves the model's ability to predict both the coverage and spatial distribution of short-term heavy rainfall.

(4) The joint assimilation of X-band radar data improves radar echo forecasts.

In the composite reflectivity forecasts, CTRL performs relatively poorly in reproducing the continuity of the main echo band and the localized intense echo cores. DA_S markedly improves the structure of the main echo band and the distribution of localized intense echo cores. Building on this, DA_S_X further enhances the representation of internal details within the banded echo structure and the localized intense echo centers. The echo BIAS results show that, under both the 20 dBZ and 40 dBZ thresholds, DA_S_X produces echo coverage closest to the observations. This indicates that the joint assimilation of X-band radar data further improves the model's ability to simulate the fine-scale echo structure of severe convective systems.

6.2 Innovations of This Study

Based on the research contents and results of this study, the main innovations can be summarized as follows.

(1) For a typical severe convective case over the middle and lower reaches of the Yangtze River, this study systematically compares the impacts of two assimilation strategies—assimilating S-band radar data alone and jointly assimilating S-band and X-band radar data—on wind-field structure, echo structure, and precipitation forecasts. In doing so, it provides a relatively comprehensive assessment of the added value of X-band radar observations in Jiangsu Province for convective-scale data assimilation.

(2) This study combines multi-radar retrieved wind-field analysis with data assimilation experiment results and establishes a relatively complete analysis chain linking observational evidence, dynamical structure, and forecast performance. This framework provides a stronger physical basis for interpreting the role of X-band radar observations.

6.3 Limitations

Although this study has obtained some meaningful results, several limitations remain.

(1) This study focuses on only one squall-line severe convective event that occurred on 1 July 2024, and the number of cases examined is therefore limited. Different types of severe convective systems differ substantially in environmental configuration, echo structure, and microphysical processes. As a result, the applicability of the conclusions presented here under broader weather conditions still needs to be tested using more cases. Future work may include comparative studies of multiple squall lines, bow echoes, supercells, and short-duration heavy-rainfall events in order to improve the generality of the conclusions.

(2) This study adopts the WRFDA 3DVar framework and an indirect assimilation scheme. Although this approach has advantages in computational efficiency and system stability, it still has limitations in representing temporal evolution and nonlinear microphysical processes. Future studies may further explore EnKF, 4DVar, or hybrid data assimilation methods, and compare the performance of

X-band radar data under different assimilation frameworks, so as to assess the potential improvement that more advanced assimilation methods may provide for severe convective weather forecasts.

(3) This study mainly focuses on forecast results in terms of wind fields, hydrometeors, composite reflectivity, and precipitation. However, the physical mechanisms through which X-band radar data improve forecasts have not yet been examined in sufficient depth. For example, the specific roles of X-band radar data in modifying low-level convergence, cold-pool structure, the evolution of upward motion, and microphysical feedback processes still require further diagnostic analysis. Future work may combine diagnostic variables such as vertical velocity, temperature and moisture structure, cold-pool evolution, and convective initiation conditions to provide a more detailed discussion of the underlying mechanisms.

References

Aksoy, A., Dowell, D. C., and Snyder, C., 2009. A multicase comparative assessment of the ensemble Kalman filter for assimilation of radar observations. Part I: Storm-scale analyses. Monthly Weather Review, 137(6), 1805–1824.

Anagnostou, E. N., Anagnostou, M. N., Krajewski, W. F., Kruger, A., and Miriovsky, B. J., 2008. High-resolution rainfall estimation from X-band polarimetric radar measurements. Journal of Hydrometeorology, 9(4), 589–606.

Bannister, R. N., 2008. A review of forecast error covariance statistics in atmospheric variational data assimilation. Quarterly Journal of the Royal Meteorological Society, 134(637), 1951–1970.

Barker, D. M., Huang, W., Guo, Y.-R., Bourgeois, A. J., and Xiao, Q. N., 2004. A three-dimensional variational data assimilation system for MM5: Implementation and initial results. Monthly Weather Review, 132(4), 897–914.

Barker, D. M., Huang, X.-Y., Liu, Z., Auligné, T., Zhang, X., Rugg, S., Ajjaji, R., Bourgeois, A., Bray, J., Chen, Y., Demirtas, M., Guo, Y.-R., Henderson, T., Huang, W., Lin, H.-C., Michalakes, J., Rizvi, S., and Zhang, X., 2012. The Weather Research and Forecasting model's community variational/ensemble data assimilation system: WRFDA. Bulletin of the American Meteorological Society, 93(6), 831–843.

Betts, A. K., 1993. The Betts–Miller scheme. In: Emanuel, K. A., and Raymond, D. J. (Eds.), The Representation of Cumulus Convection in Numerical Models. Meteorological Monographs, 24(46), 107–121.

Bouttier, F., and Courtier, P., 1999. Data Assimilation Concepts and Methods. ECMWF Meteorological Training Course Lecture Series, Reading, United Kingdom.

Brousseau, P., Berre, L., Bouttier, F., and Desroziers, G., 2011. Background-error covariances for a convective-scale data-assimilation system: AROME-France 3D-Var. Quarterly Journal of the Royal Meteorological Society, 137(655), 409–422.

Chen, S.-H., and Sun, W.-Y., 2002. A one-dimensional time dependent cloud model. Journal of the Meteorological Society of Japan. Series II, 80(1), 99–118.

Chen, Y., Wang, H., Sun, J., Zhang, Y., Tong, M., and Li, X., 2024. Improving forecasts of the “21·7” Henan extreme rainfall event with hydrometeor background error covariance in rapid-updated radar reflectivity assimilation. Monthly Weather Review, 152, 1651–1674.

Cheng, Y., et al., 2020. Observation capability of X-band phased array radar for convective storms. Atmospheric Research, 241, 104957.

Derber, J., and Bouttier, F., 1999. A reformulation of the background error covariance in the ECMWF global data assimilation system. Tellus A: Dynamic Meteorology and Oceanography, 51(2), 195–221.

Diss, S., Berne, A., and Germann, U., 2009. X-band radar observations of precipitation microstructure. Journal of Applied Meteorology and Climatology, 48(6), 1297–1313.

Honda, T., et al., 2022. Assimilation of phased array weather radar data for short-term precipitation forecasting. Monthly Weather Review, 150(5), 1121–1139.

Hong, S.-Y., and Lim, J.-O. J., 2006. The WRF single-moment 6-class microphysics scheme. Journal of the Korean Meteorological Society, 42(2), 129–151.

Hu, M., Xue, M., and Brewster, K., 2006. 3DVAR and cloud analysis with WSR-88D Level-II data for the prediction of the Fort Worth, Texas, tornadic thunderstorms. Part I: Cloud analysis and its impact. Monthly Weather Review, 134(2), 675–698.

Hu, M., Xue, M., Gao, J., and Brewster, K., 2006. 3DVAR and cloud analysis with WSR-88D Level-II data for the prediction of the Fort Worth, Texas, tornadic thunderstorms. Part II: Impact of radial velocity analysis via 3DVAR. Monthly Weather Review, 134(2), 699–721.

Jiménez, P. A., Dudhia, J., González-Rouco, J. F., Navarro, J., Montávez, J. P., and García-Bustamante, E., 2012. A revised scheme for the WRF surface layer formulation. Monthly Weather Review, 140(3), 898–918.

Kepert, J., 2018. The dynamics of boundary layer processes in convective systems. Journal of the Atmospheric Sciences, 75(1), 181–199.

Li, Z., Pu, Z., Sun, J., and Lee, W.-C., 2014. Impacts of 4DVAR assimilation of

airborne Doppler radar observations on numerical simulations of the genesis of Typhoon Nuri (2008). Journal of Applied Meteorology and Climatology, 53(10), 2325–2343.

Liu, L. P., Wu, L. L., Wu, C., et al., 2014. Field experiment of convective-process observations using X-band phased-array weather radar and preliminary analysis of the results. Chinese Journal of Atmospheric Sciences, 38(6), 1079–1094.

Michel, Y., Auligné, T., and Montmerle, T., 2011. Heterogeneous convective-scale background error covariances with the inclusion of hydrometeor variables. Monthly Weather Review, 139(9), 2994–3015.

Morotomi, K., et al., 2020. Observation of convective storms using X-band phased array radar. Journal of Atmospheric and Oceanic Technology, 37(8), 1363–1381.

Pereira, M. B., and Berre, L., 2006. The use of an ensemble approach to study the background-error covariances in a global NWP model. Monthly Weather Review, 134(9), 2466–2489.

Radhakrishnan, C., Chandrasekar, V., and Lim, S., 2020. CASA prediction system over Dallas–Fort Worth urban network: Implementation of radar data assimilation with WRF-3DVAR CV7. Journal of Atmospheric and Oceanic Technology, 37(2), 273–292.

Skamarock, W. C., and Klemp, J. B., 2008. A time-split nonhydrostatic atmospheric model for weather research and forecasting applications. Journal of Computational Physics, 227(7), 3465–3485.

Skamarock, W. C., Klemp, J. B., Dudhia, J., Gill, D. O., Liu, Z., Berner, J., Wang, W., Powers, J. G., Duda, M. G., Barker, D. M., and Huang, X.-Y., 2019. A Description of the Advanced Research WRF Model Version 4.1. NCAR Technical Note.

Song, G., Lei, L., Ma, J. L., et al., 2022. Characteristics and applications of X-band dual-polarization radar in severe convective weather in Beijing. Mid-Low Latitude Mountain Meteorology, 46(6), 63–69.

Song, G., et al., 2022. Microphysical characteristics of convective storms observed by X-band dual-polarization radar. Atmospheric Research, 270, 106072.

Song, W., Xue, M., and Liu, S., 2023. Comparison of different momentum control variables on radar data assimilation and convective precipitation forecasting in WRFDA. Frontiers in Earth Science, 11, 1148921.

Sun, J., Xue, M., Wilson, J. W., Zawadzki, I., Ballard, S. P., Onvlee-Hooimeyer, J., Joe, P., Barker, D. M., Li, P.-W., Golding, B., Xu, M., and Pinto, J., 2014. Use of NWP for nowcasting convective precipitation: Recent progress and challenges. Bulletin of the American Meteorological Society, 95(3), 409–426.

Sun, J., Wang, H., Tong, W., Zhang, Y., Lin, C.-Y., and Xu, D., 2016. Comparison of the impacts of momentum control variables on high-resolution variational data assimilation and precipitation forecasting. Monthly Weather Review, 144(1), 149–169.

Wan, S., Zhang, F., and Liu, Y., 2024. Evaluation of two momentum control variable schemes in WRFDA for convective-scale radar data assimilation. Atmosphere, 15(3), 342.

Wang, C., Zhao, K., Zhu, K., et al., 2021. Assimilation of X-band phased-array radar data with EnKF for the analysis and warning forecast of a tornadic storm. Journal of Advances in Modeling Earth Systems, 13(10), e2020MS002441.

Wang, X., Barker, D. M., Snyder, C., and Hamill, T. M., 2008. A hybrid ETKF–3DVAR data assimilation scheme for the WRF model. Part I: Observing system simulation experiment. Monthly Weather Review, 136(12), 5116–5131.

Wang, X., Barker, D. M., Snyder, C., and Hamill, T. M., 2008. A hybrid ETKF–3DVAR data assimilation scheme for the WRF model. Part II: Real observation experiments. Monthly Weather Review, 136(12), 5132–5147.

Wang, X., and Wang, Y., 2021. Development of convective-scale static background error covariance within GSI-based hybrid EnVar system for direct radar reflectivity data assimilation. Monthly Weather Review, 149(8), 2713–2736.

Wang, Y., Min, J., Chen, Y., and Huang, X.-Y., 2017. Improving precipitation forecast with hybrid 3DVar and time-lagged ensembles in a heavy rainfall event.

Atmospheric Research, 183, 1–16.

WRF Users Page, 2026. Chapter 6: WRF Data Assimilation (WRFDA). NCAR/MMM User Guide.

Wu, Z., and Liu, L., 2014. Multi-radar observations of convective storms in China. Advances in Atmospheric Sciences, 31(2), 457–469.

Xiao, L., et al., 2021. Evaluation of low-level radar observation capability for convective storms. Advances in Atmospheric Sciences, 38(8), 1295–1308.

Xiao, Q., Kuo, Y.-H., Sun, J., Lee, W.-C., Lim, E., Guo, Y.-R., and Barker, D. M., 2007. An approach of radar reflectivity data assimilation and its assessment with the inland QPF of Typhoon Rusa (2002) at landfall. Journal of Applied Meteorology and Climatology, 46(1), 14–22.

Zhang, F., Snyder, C., and Sun, J., 2008. Impacts of Doppler radar observations on storm-scale analysis. Monthly Weather Review, 136(3), 1046–1063.

Zhang, G., Mahale, V. N., Putnam, B. J., et al., 2019. Current status and future challenges of weather radar polarimetry: Bridging the gap between radar meteorology/hydrology/engineering and numerical weather prediction. Advances in Atmospheric Sciences, 36(6), 571–588.

Zhang, X., Bao, J. W., Chen, B., and Grell, E. D., 2018. A three-dimensional scale-adaptive turbulent kinetic energy scheme in the WRF-ARW model. Monthly Weather Review, 146(7), 2023–2045.

Zhang, Y., et al., 2020. Multi-radar data assimilation for convective storms. Journal of Meteorological Research, 34(2), 412–427.

Zhang, Z., et al., 2021. Comprehensive observation of a mesoscale convective system using phased array radar. Atmospheric Research, 250, 105378.

Zhao, Q. Y., and Jin, Y., 2008. High-resolution radar data assimilation for Hurricane Isabel (2003) at landfall. Bulletin of the American Meteorological Society, 89(9), 1355–1372.

Zhu, D., Gu, J. X., Shi, C. X., et al., 2018. Analysis of effective coverage and terrain blockage in the network design of China’s new-generation weather radar. Meteorological Monthly, 44(11), 1434–1444.

Acknowledgements

As this thesis is nearing completion, my graduate study is also coming to an end. Looking back on this period, from topic selection and data collection to experiment design, result analysis, and thesis revision, I have received much care, help, and support. It is because of this support that I have been able to complete my studies and this thesis successfully. I would therefore like to express my sincere gratitude to everyone who has helped and supported me along the way.

First, I would like to thank my supervisor for the patient guidance and careful support provided throughout this research. From refining the research ideas and designing the experiments to analyzing the results and revising the thesis, a great deal of time and effort was devoted to this work. My supervisor's rigorous academic attitude, practical research style, and thoughtful approach to scientific problems have deeply inspired me and have helped me continuously improve my understanding and research ability.

Second, I would like to thank the teachers in my school and research group for their guidance during my study and research. The coursework and research training during my graduate study have helped me further improve my professional knowledge, research methods, and academic writing skills. Their responsible teaching attitude and rigorous academic spirit have had a profound influence on me.

I would also like to thank my fellow students in the laboratory and research group for their help in study, research, and daily life. Whether in data processing, code debugging, problem discussion, or thesis revision, they have given me much support and inspiration. The experience of studying, communicating, and making progress together with them has become a valuable memory of my graduate years.

I am grateful to the university and the school for providing a good platform and supportive conditions for study and research, which enabled me to complete this work in a favorable academic environment.

Finally, I would like to express my special thanks to my family for their understanding, companionship, and support throughout this period. It is because of

their encouragement and tolerance that I was able to remain confident when facing difficulties and pressure, and to persist in completing this stage of my academic work.

With these words, I would like to extend my heartfelt thanks to all the teachers, classmates, friends, and family members who have cared for, helped, and supported me.